ABSTRACT

Title of Thesis: EXPLORING AN ALTERNATIVE TECHNOLOGY FOR MANUFACTURING ELECTRONICS FOR EXTREME TEMPERATURES

Mital Raju Patel, Master of Science Mechanical Engineering, 2023

Thesis Directed by: Dr. Patrick McCluskey, Mechanical Engineering

Within our increasingly digital world, there is a demand to integrate electronics into every industry to take advantage of applications in communication, optimization, and artificial intelligence. Relatively untapped areas for electronics implementation are the extreme environments where high temperatures (>300°C) are present. These environments are common within energy, automotive, and aerospace industry es. Current high temperature technologies limit reliable use of electronics to ~200°C. Emerging technologies, such as transient liquid phase (TLP) bonding, copper sintering, and thick films, have not yet demonstrated resilient operation above 300°C. Possessing various remarkable properties, diamond is a promising material that can be used in manufacturing electronic devices operable well above 500°C. Graphene and

graphite additionally can serve as conductive material for circuitry or other electronic elements. The compatibility and versatility of these three materials demonstrate the potential for robust, all-carbon electronics for high temperature applications. Chemical vapor deposition (CVD), the predominant method of synthesizing diamond for electronics, involves very costly, long processes at extreme temperatures. A relatively underdeveloped, alternative method utilizes the pyrolysis of polymer precursors into diamond. This study aims to further explore this method using Poly(naphthalene-co-hydridocarbyne) (PNHC). The polymer synthesis, processing, and pyrolysis have been performed here, and the process parameters and outcomes at each step have been documented. Native graphite and graphene growth on diamond surfaces allows for the integration of conductive material on insulating diamond. Four known methods of diamond graphitization, assisted with the metal catalysts nickel, copper, and iron, have also been applied to support the fabrication of carbon-based electronics. Ultimately in this study, the synthesis of diamond has been unsuccessful, but multi-layer graphene has been grown on polycrystalline diamond with high sheet carrier concentration and mobility values of $1.0*10^{15}$ cm^{-2} and 629.1 cm^2 Vs^{-1}, respectively.

EXPLORING AN ALTERNATIVE TECHNOLOGY FOR MANUFACTURING ELECTRONICS FOR EXTREME TEMPERATURES

by

Mital Raju Patel

Thesis submitted to the Faculty of the Graduate School of the
University of Maryland, College Park, in partial fulfillment
of the requirements for the degree of
Master of Science
2023

Advisory Committee:

Professor Patrick McCluskey, Chair

Associate Professor Damena Agonafer

Associate Professor Ryan Sochol

Table of Contents

1. Chapter 1: Review of Current High Temperature Electronics Technology

1.1 Introduction

Electronics for high temperature applications require designs capable of enduring extreme stresses and large temperature swings while maintaining reliable function. Relevant demanding environments are present in the automotive, aerospace, and oil and gas industries, especially in cases where limitations are placed on thermal management strategies. Temperatures in these applications range from >200°C in automobiles to >300°C in jet engines and >500°C for space applications [1]. size, cost, and material limitations are great challenges in these environments, as well as being relevant to modern high power and high heat flux electronics. High temperature cycling and operation induce significant stresses and inelastic strain. Additionally, critical, low maintenance, and long lifetime electronics systems necessitate highly reliable designs. However, the reliability of electronics often decreases significantly with increasing temperature. Most conventional materials and manufacturing processes appear to be limited to functioning at 300°C, even without considering designing for reliability. As a result, there exists a need to make use of more robust materials. The current thermal capabilities of some contemporary electronic material technologies are briefly discussed here.

1.2 Resistors

1.2.1 Wirewound Resistors

The core components of wirewound resistors are a resistive wire wound around an alumina-based ceramic core with gold-plated nickel end caps. These resistors are among the least noisy and are great for high power applications. The resistive wire can be made of different alloys with known temperature-dependent resistances, notably nickel-chromium, copper-nickel,

copper-manganese, and iron-chromium, and the size of the ceramic core varies with power levels [2]. The materials for the molding and housing for these parts have high thermal stability. Individually, the materials for wirewound resistors can survive temperatures up to 400°C, but they are often derated to no more than 300°C [1, 3]. High temperature baking at 300°C for 10,000 hours has been tested to shift the resistance of some wirewound resistors by <4% [3]. Testing with 1,000 cycles from -55°C to 225°C [3] and from -55°C to 275°C [4] has shown that these resistors are able to withstand high temperature thermal cycling, although some damage, such as microcracking, is likely to occur [3].

1.2.2 Thick Film Rectangular Chip Resistors (Surface Mount Technology)

Rectangular chip resistors are ~100 μm thick films of a mixture of glassy materials and metal oxides [2]. Generally being sized in mils for each dimension, these resistors can be very small in size. Since they are manufactured at temperatures ranging from 500°C-1,000°C, rectangular chip resistors have great theoretical thermal stability. In testing, resistances of differently rated thick film resistors shift by ~3% after 10,000 hours of aging at 300°C and are generally not rated for much higher temperatures [3].

1.3 Capacitors

Most polymer dielectrics for capacitors breakdown above 200°C, but polymers such as PTFE, FDAPE, PBO copolymer, and PI-ADE have been found to maintain capacitance after heating to 250°C [5]. One alternative to polymer dielectrics is lead zirconate titanate (PZT) film which possesses a parabolic temperature-dependent capacitance curve well above 300°C [6]. Another alternative is ceramic dielectrics; one new high temperature, high permittivity ceramic is $0.6Bi_{1/2}Na_{1/2}TiO_3–0.4Bi_{1/2}K_{1/2}\ TiO_3$ (BNT–0.4BKT) modified with KNN. This material is

thermally stable up to at least 400°C and possesses a temperature-dependent permittivity that plateaus around 350°C [7].

1.4 Device Attach

1.4.1 Solder

Solders are metal alloys used widely in electronics for device attach applications. Some solders have been formulated with melting temperatures well above 300°C; a list of some solder melting temperatures is given in Table 1 below. The limitations, however, for implementing solder technology in high temperature applications depend on the solder and may include intermetallic formation, poor thermal cycling resistance, poor manufacturability, low thermal conductivity, high cost, environmental impact (notably for lead-based solders), low mechanical strength, tin whisker formation, electromigration, and highly temperature-dependent properties [8-11].

Material	Solidus Temperature or Melting Point(°C)	Reference
Sn–65Pb	183	[12]
Sn–70Pb	183	[12]
Sn–80Pb	183	[12]
Sn–90Pb	268	[12]
Sn–95Pb	300	[12]
Sn–98Pb	316	[12]
Sn-3.5Ag	221	[13]
Sn-5.0Au	215-217	[16]
Sn-25Ag-10Sb	233	[13]

Sn-5.0Sb	235	[13]
Au–20Sn	280	[13]
Au–0.28Ge	360	[14]
Au-12Ge	365	[15]
Au-3.15Si	363	[15]
Au-30Ga	450	[15]
Au-19In	487	[15]
Bi–2.5Ag	262.5	[17]
Bi–10Ag	261.4	[18]
Zn–6Al	381	[12]
Zn–4Al–3Mg–3.2Ga	309	[19]
Zn–20Sn	198	[2]
Zn–30Sn	198	[20]
Zn–40Sn	198	[20]
Pb-10.0In	260	[13]
Pb-5In-2.5Ag	300	[13]
Pb-5.0Sn	308	[13]
Pb-5.0Sn-2.5Ag	287	[13]

Table 1: A list of some high temperature solders and their melting points

1.4.2 Transient Liquid Phase (TLP) Systems

Transient liquid phase systems constitute melting a lower melting point metal and allowing it to diffuse into a second solid metal that has a higher melting point at a temperature slightly above that lower melting point. This results in an intermetallic possessing a higher melting point than the processing temperature. Because of the high final melting point relative to the processing temperature, considerable research is focused on these intermetallics as die attach

materials for high temperature applications. Due to the formation of different intermetallics, variable intermetallic diffusion, oxidation, and wetting, the strength and reliability of TLP systems is a continuously studied field. Ni-Sn TLP bonds have been shown to be mechanically and electrically resistant towards 1,000 thermal cycles between -40°C and 200°C [21]. Ni-Sn3.5Ag joints were tested to be mechanically sound, despite containing small cracks, after 500 hours of thermal aging at 185°C and subsequent dropping 1000 times with a load of 1500 g [22]. For higher temperatures, tin - gold based TLP systems may have melt temperatures up to 800°C [23]. One study found using a sacrificial nickel layer prevented intermetallic formation between copper and Ag_3Sn bonds, allowing operation even after 1,000 hours of aging at 350°C [24]. The strength of Ag_3Sn bonds was further investigated in a later study analyzing the effect of supplementing silver joints with tin. The shear strength for Ag_3Sn bonds increased over time when aged at 200°C, but it decreased with time when aged at 300°C as well as with increasing thermal cycles between -40 and 150°C [25]. However, it should be noted that, unlike the previous study, no nickel sacrificial layer was used. As a lower cost alternative, TLP systems using copper are a subject of focus as well. Copper-based TLP systems functional at 400°C and 600°C [26]. TLP joints formed from Ag20Sn, Cu40Sn, and Cu50Sn maintained similar or higher shear strengths at 400°C compared to room temperature, with Cu40Sn maintained a high shear strength at 600°C [27]. Another copper system, Cu-In, tested to have shear strengths that were maintained, if not increased, after 500 hours of storage at 500°C and 500 thermal cycles between -40 and 125°C [28]; however, cracks and voids form after thermal cycling.

1.4.3 Sintered Silver

Sintered silver technology has also been developed as an alternative to solder. Sintered silver possesses higher thermal conductivity, lower electrical resistance, and higher strength than solder. It can be used as a drop-in replacement for solders as well. The disadvantages of sintered silver include high cost, a lack of self-aligning capabilities, risk of silver migration, and the requirement for silver plated surfaces for best use. There are two types of silver sinter pastes – silver microflake paste and silver nanopowder paste. Silver microflake paste requires high pressures (30-40 MPa). On the other hand, silver nanopowder paste can be applied in an inert atmosphere environment. The toxicity of nano-silver particles, however, is currently unknown.

The high temperature performance of sintered silver is currently being investigated. Manufacturing methods are being studied to determine what conditions limit porosity and in turn improve bond integrity. Sintering nanosilver paste in a nitrogen atmosphere leads to higher shear strengths compared to sintering in air [29]. Increasing pressure during the sintering process to 30 MPa produces shear strengths over 70 MPa [30]. Power cycling of sintered silver on direct bonded copper with a temperature range of 130K and a max temperature of 175°C results in power module lifetimes 17 times longer than with soldered or wire bonded connections on direct bond copper and 2.7 times longer for similar bonds on direct bond aluminum [31]. The aging characteristics under high temperature has been documented for sintering on different substrates [32]; for example, sintered silver previously maintained shear strengths up to 225°C after aging of 500 hours. One novel method for improving sintered silver bond reliability utilizes pre-sintered layers of silver on direct bond aluminum substrates, resulting in joints that survive 900 thermal cycles from -45°C to 250°C with minimal change to silver grain size [33].

1.4.4 Sintered Copper

Sintered copper is a promising alternative to solder and sintered silver. Sintered copper melts at over 1,000°C, has comparably high thermal and electrical conductivities, is less expensive than silver, and is less prone to migration. Oxidation and high process temperatures are the primary weaknesses of sintered copper. Sintering under pressure and in an inert atmosphere are also potential drawbacks depending on the specific copper paste. Studies have demonstrated the viability for sintered copper die attach (shear strengths >30 MPa) with process temperatures of 230°C to 275°C under a nitrogen or other inert atmosphere and under pressure [34-36,29-30]. Shear strengths tend to increase with increasing bonding pressure [34], but some pastes may produce adequate shear strengths when processed pressure-less [35]. One study demonstrated successful sintering in air with copper nanopaste [37]. Furthermore, sintered copper exhibits good reliability performance. Thermal cycling performance has been shown to be at least 10 times better than conventional solders [38], and sintered copper specimens have survived on the order of 10^4 cycles of 160 MPa stresses, depending on bonding pressure [39]. Compared to sintered silver joints, sintered copper joints have better creep and fatigue strength [40, 41, 42], better thermal cycling resistance [40, 43, 44], better thermal shock resistance [40, 45, 46], and better power cycling performance [40]. However, sintered copper possesses lower electrical and thermal conductivity, requires higher processing temperatures, and will form Kirkendahl voids [40, 47]. In addition to die attach applications, sintered copper is a promising interconnect material, especially in 3D packaging designs, as the electrical conductivity of sintered copper interconnects have been shown to be 82% higher than that of conventional solder [48].

1.5 Substrate Technology

1.5.1 Overview

Mechanical, electrical, and thermal properties of ceramics must be considered for specific applications. In particular, the thermal conductivity and CTE of substrates need to be balanced with those of other materials while also considering strength and thermal conductivity. Table 2 lists various relevant properties of four commonly used ceramics [49].

	Al_2O_3	AlN	Si_3N_4	BN
Thermal Cond. [W/mK]	26-35	150-180	20-30	20-60
CTE [ppm/°C]	6.8-9	4.3-6.2	2.6-3.6	0.1-6
Flexural Strength [MPa]	300-400	300-350	500-800	20-90
Dielectric Strength [kV/mm]	<10	14-17	16-20	40-200

Table 2: Properties of Alumina, Aluminum Nitride, Silicon Nitride, and Boron Nitride

Table 3 summarizes different ceramic substrate technologies. Printed metallization uses metal pastes that are sintered at elevated temperatures while bonded metallization uses bulk metallic structures that are fused with ceramics. Pre-fired ceramics refer to the use of green tapes that are sintered simultaneously with metal pastes, and post-fired ceramics refer to those that were sintered before the application of metal.

Ceramics	**Metallization**	
	Printed	**Bonded**
Pre-fired	• Low Temperature Cofired Ceramics (LTCC) • High Temperature Cofired Ceramics (HTCC)	none
Post-fired	• Copper Thickfilm • Silver Thickfilm	• Direct Bond Copper (DBC) • Direct Bond Aluminum (DBA) • Active Metal Brazed (AMB)

Table 3: Overview of Different Substrate Technology

1.5.2 DBC, DBA, and AMB

Direct bond copper (DBC) is the oxide bonding of copper on alumina or aluminum nitrate. Debonding of the metallization may occur due to CTE mismatch between copper and the ceramic during temperature cycling. This can be mitigated slightly with dimpling or thinning of the metallization and bonding the substrate to a heatsink. Studies have shown that DBC substrates typically fail thermal cycling tests with temperature ranges of ~300K in only 20-30 cycles [50-53], but substrates with stepped edges sealed in epoxy survive to prevent delamination for over 850 cycles [52]. Active metal brazed ceramics (AMB) substitutes alumina or aluminum nitrate with silicon nitride for higher fracture toughness. Thinner silicon nitride layers can be used for lower thermal resistance. AMB is still susceptible to peeling and delamination, though.

AMB substrates have shown to survive 1,000 thermal cycling tests ranging from -55° been shown 250°C [54-56]. Direct bond aluminum (DBA) faces a different problem of hillock formations causing short circuits when stresses over 20 MPa are present. However, DBA substrates have demonstrated higher resilience, as they can survive 1,500 cycles from -55°C to 250°C [57].

1.5.3 Thick Film Substrates

Copper and silver thick films are created from stencil printing metal paste on pre-sintered ceramic substrates. Copper paste is sintered at 600°C-900°C in an N_2 atmosphere while silver paste is sintered around 850°C; however, efforts have recently found methods of copper sintering at 500°C [58]. Both thick films can be used in alumina and aluminum nitride ceramic systems. Layer thicknesses of copper and silver films range between 20-60µm and 25-30µm, respectively, and films can be built up to 300 µm. The creation of vias for both thick films is unfortunately difficult. These thick films are used in power modules, high brightness LED packaging, solid state power circuits, battery chargers, and electronic heating devices. Thick copper films on aluminum nitride survive over 3,000 cycles between -40°C and 150°C [59] and well over 400 cycles between 0°C and 350°C [51]. Silver thick films last from 181 to over 500 cycles between the latter range, depending on film thickness [51].

The advantages copper and silver thick film ceramics have over direct bond copper or direct bond aluminum ceramics include higher thermal cycling reliability, additive manufacturing processes, improved spatial resolution, the possibility of through-substrate contacts, and variable layer thickness. The disadvantages include limited supplier support, no bulk metallization, multiple extra steps for very thick metallization (>200 µm), higher costs, and lower current carrying capability.

1.5.4 Epoxy Resin Composite Dielectric (ERCD)

Epoxy resin composite dielectric (ERCD) substrates are a lower cost alternative to direct bond copper and other ceramic substrates. These substrates use high temperature epoxy resin instead of ceramics, leading to a more flexible substrate whose CTE matches that of copper more closely [60]. ERCD substrates possess higher thermal performance and better reliability compared to direct bond copper on alumina [61-62]. The breakdown voltage and peel strength of ERCD has been tested to remain constant after 3,000 hours of aging at 175°C and 3,000 thermal cycles from -40°C to 125°C [63]. In identical cases, the mechanical stresses present within ERCD are lower compared to alumina and aluminum nitrate, and solder fatigue life on ERCD is greater [63]. ERCD substrates have not been used or widely tested, and the limits of the technology may depend on the constituent material limits. The maximum temperature limit is currently ~300°C, which is the glass transition temperature of common epoxies used [60].

1.5.5 Metal Core Printed Circuit Boards (MCPCB) and Insulated Metal Substrates (IMSs)

Metal core printed circuit boards (MCPCBs) have substrates based on a metal core and heat sink with sandwiched dielectric layers. MCPCBs are generally used in high heat generation applications such as LEDs because, compared to other substrates, they have higher thermal conductivities and dissipate heat more efficiently [64]. Improvements on the standard MCPCB format include embedded heat pipes [65], and diamond particles or layers [66-67]. Although reliability studies have been performed on LEDs with MCPCB packaging [64, 68], research into thermal cycling or thermal aging on MCPCB substrates is lacking.

Insulated metal substrates (IMS) are an assembly of polymer films that insulate metal layers. IMS does not possess significantly better steady state thermal performance compared to direct bond copper, but it does have up to 40% improvement in die temperatures in transient heat

transfer [69-71]. IMS exhibits a 45-70% reduction in thermal resistance compared to FR-4 PCBs [71-72]. The substrate possesses good thermal reliability performance, working best with epoxy, as it did not present failures when cycled between -55°C and 150°C 1,000 times or when the junction temperature was cycled in range of 100K 15,000 times in one study [73]. More rigorous testing on IMS has not been performed, although some commercial IMS claim to operate up to 300°C [74].

1.5.6 Diamond Films

Diamond is a notable material in the field of power electronics and known for its excellent strength, high decomposition temperature, great thermal conductivity, and high dielectric strength. The former two properties place diamond as the ideal heat spreading material. Diamond can also be doped to be made into conducting diamond, semiconductors, transistors, and diodes [75]. The deposition of diamond films requires high power plasma enhanced chemical vapor deposition and very high temperatures reaching well over 1,000°C. This makes diamond processing for high power electronics difficult and costly. Diamond-like carbon, although less useful, on the other hand has been manufactured at temperatures as low as 300°C [76].

1.6 Encapsulation

1.6.1 Epoxy and Silicone Sealants

A wide variety of epoxy compounds are commercially available and rated to 200°C, and only but a few can be used above 300°C. Cyclotene 4000 from Kayaku Advanced Materials, silicone products from CHT-Silicones, and several Masterbond epoxy solutions are rated for

>300°C. One issue with epoxy is outgassing, especially at high temperatures. NASA has a public database detailing outgassing metrics for different epoxy.

1.6.2 Ceramic Potting

Potting technology provides extra mechanical protection to electronic components from the environment. Temperature resistant ceramic potting materials are commercially available. Two materials of note are Ceramcast from Aremco and Durapot from Cotronics. Several potting materials, some rated to withstand 1,500°C, are available and vary in curing method, binding systems, thermal properties, and electrical properties.

1.6.3 Coatings

Parylene HT is a coating solution for high temperature electrical insulation. This coating is applied using chemical vapor deposition. Parylene HT coating demonstrates good temperature stability up to 400°C. Polyimide is another material useful for coating electronics. A thin film of polyimide can resist environments up to 400°C and has good anti-corrosion properties. Commercial electronic coatings are also available, such as Duralco 4460, which is a two-part coating rated to 315°C.

1.7 Conclusion

Both mature and new technologies for high temperature electronics applications have been reviewed. The current operating temperatures for electronics exceed 200°C and approach 300°C, depending on the device. However, material properties and joint integrity over 300°C decline in most cases. As a result, new materials that are stable up to 500°C need to be identified. One emerging high temperature technology is synthetic diamond, possessing remarkably high thermal conductivity and mechanical strength. Considering the current diamond manufacturing

processes are relatively costly, often complex, and require extreme environments, the use of diamond is very limited. However, its superior material properties warrant a closer look. A review of diamond manufacturing and applications is present in Chapter 2.

2. Chapter 2: Review of Manufacturing Methods of Diamond for Electronics Applications

2.1 Introduction

Diamond is a promising high temperature material with a plethora of potential electronic applications. The thermal limitation of diamond is the process of burning when exposed to an oxygen atmosphere above 600°C [79]. High temperature semiconductors that operate at comparable temperatures, such as silicon carbide and gallium nitride, already exist and are used in industry [80]. Compared to alternative semiconductors, diamond has a higher bandgap (5.5 eV), a higher carrier mobility (2,000 $cm^2\ V^{-1}\ s^{-1}$), and overall the highest Baliga's figure of merit ($9.7*10^5$) [75], which makes diamond a promising semiconductor for power electronics. Additionally, the versatility of diamond warrants attention. Having a thermal conductivity of 2,000W/mK and a dielectric strength of 1000 kV/mm [81], ordinary diamond serves as a superb thermal conductor and an electrical insulator. The strength and hardness of diamond is exceptional, and it is chemically inert. Boron and phosphorous also allow diamond to become a p-doped or n-doped, respectively, electrically conductive material. Uses for diamonds in high temperature electronics and other applications include Schottky diodes, transistors, radiation detectors, and quantum sensors. The manufacturing and processing techniques for synthesizing and preparing diamond for electronics applications are presented in this chapter.

2.2 High Pressure High Temperature (HPHT)

2.2.1 Technology Overview

High pressure, high temperature (HPHT) growth of diamond involves growing diamond at pressures of 5 GPa and at temperatures 1,500°C or higher, depending on the synthesis method [75]. These conditions lie passed the metal-carbon eutectic line and away from the graphite

stable region in the carbon phase diagram [82]. HPHT techniques are costly and usually result in cubooctahedral crystals no larger than a few centimeters, and more often on the order of micrometers and millimeters, in their largest dimensions. As a result, although HPHT growth methods are the most widely used in other industries, they are not ideal for electronics manufacturing.

2.2.2 Solubility-Gradient Method

The solubility-gradient method involves mixing carbon in molten metals such as nickel, cobalt, iron, tantalum, and chromium and subsequently subjecting the solution to HPHT conditions [83]. This method primarily produces diamond powders and crystals no larger than 1mm in size [82]; however, the growth rate of these crystals can be over 0.1 mm/minute [83]. The growth processes occur within the molten metal matrix, but the catalyzation and crystal growth only occurs in a region very close to the carbon-metal interface, preventing the formation of larger crystals.

2.2.3 Temperature-Gradient Method

The temperature-gradient method utilizes a catalytic metal solution sandwiched between a carbon source and a diamond seed. This system is first loaded into a high pressure (~5.5 GPa) cylinder and piston apparatus and subsequently heated up to a temperature between 1,300-1,400°C [82]. A temperature gradient (20-50°C) between the hotter carbon source and the cooler diamond seed forms, creating a supersaturated carbon solution at the diamond seed. The resulting growth at the diamond seed depends on factors such as the temperature gradient [84] and geometry of the diamond seed [85]; growth rates typically do not exceed 5 mgh^{-1}. A diamond crystal major dimension of over 1 cm has been achieved using this method [86].

2.2.4 Direct HPHT Conversion

Diamond formation without the use of catalysts employs a carbon source comprised of graphite, diamond powder, or one of a variety of other pure carbons or organic compounds at pressures commonly exceeding 10 GPa and temperatures up to 2,700°C [87]. Direct conversion of graphite over 15 GPa and between 2,100°C and 2,400°C forms nanocrystalline diamond. Lower temperatures or pressures result in incomplete conversion or the formation of lonsdaliete. Diamond sintering of diamond powder requires different pressures and temperatures dependent factors such as powder size [87]. These parameters may range from 7 GPa and 1,300°C to 16 GPa and 2,300°C. Sufficiently high temperatures and pressures are required to not only facilitate the integration of grain boundaries through plastic deformation and pyrolysis but also to prevent conversion back into graphite. Using this method, ~700 mm^3 ultra-strong diamond parts have been formed [88]. One study also found that including ethanol into the diamond powder results in high purity diamond at relatively lower pressures and temperatures [89].

2.2.5 Hydrothermal Method

Hydrothermal techniques of growing diamond originally based synthesis off natural diamond formation. Carbon-containing water solutions are subjected to pressures and temperatures ranging from <1 GPa and <800°C to >5 GPa and >2,000°C [87, 90]. Diamond growth occurs typically on the order of hours or days, depending on temperature, the presence of diamond or graphite seeds, and solution. Hydrothermal methods of growing diamond are limited by small diamond crystal growth (<10 μm), difficulty to control solution concentrations, lack of complete understanding of diamond growth, poor repeatability for some techniques, low yield, and often long growth times.

2.2.6 Shock Wave Synthesis

Diamonds formed from shock waves can be up to 720 mm^3 in size [87, 91]. When carbon sources, typically graphite, are subjected to an explosion, the yield is rather low. On the other hand, detonating carbon-containing explosives results in higher yields. Tested explosives include TNT, TH50/50, RDX, HMX, and BTF. The explosion occurs in water to cool diamond as to prevent it from graphitizing. Diamond particulate must be purified and extracted from the resulting residue afterwards. Another similar method is diamond sintering of powder though shock [91]. Large starting grain sizes as well as inhomogeneous temperature distributions produce significant cracking for this method.

2.3 Chemical Vapor Deposition (CVD)

2.3.1 Technology Overview

The chemical vapor deposition (CVD) of diamond films primarily consists of growing diamond vertically in a reactor containing a carbon-based gas, usually methane, under low pressure (< 1 atm) with substrate temperatures exceeding 1,000°C and gas temperatures exceeding 3,000 °C [75]. Hydrogen is supplemented into the reactor for surface termination and graphitization inhibition [92, 93] as the high gas temperature splits molecular hydrogen into atomic and ionized hydrogen. Oxygen presence is also necessary for diamond growth, and the concentrations of carbon, hydrogen, and oxygen needed are dependent on CVD process and crystal orientation.

The ability to grow well-defined, pure films of known thickness makes CVD the preferred technology over HPHT regarding electronic device fabrication. The high temperatures and high cost of the growth process, however, provide challenges for using diamond, especially

when integrating with other materials. The current objectives in CVD diamond growth research include improving growth rates, lowering defect density, increasing wafer size, lowering process temperatures, and increasing dopant concentrations.

2.3.2 Types of CVD for Diamond Growth

2.3.2.1 Hot Filament CVD

There are several types of CVD for diamond growth. Hot filament CVD (HFCVD) employs a heating element placed 5-20 mm from the substrate to heat gas to ~2,000K [92]. The heating element, typically a filament or a graphitic rod, is maintained at 2,600K as gas flows over it at a pressure between 0.4-14 kPa. This allows the substrate to heat to 1,000-1,200K. The gas composition and process parameters depend on filament type (filament vs graphitic rod) and stage of the process (nucleation vs growth); for example, methane is not used, only hydrogen, when a graphitic rod is used due to the preferential formation of graphite on the substrate [93, 94]. Studies demonstrate diamond quality and growth rate depend on pressure [95], substrate temperature [96], and carbon source [94]. Advantages of HFCVD include relatively lower costs, high diamond quality, potential for better doping concentrations while disadvantages include lower growth rate and filament degradation over time [92, 93].

2.3.2.2 Combustion or Chemically Assisted CVD

Another CVD method that relies on direct heating of the gas is combustion assisted CVD or chemically activated CVD (CACVD). The combustion is an exothermic process between oxygen and acetylene that results in a flame with a temperature between 2,000K and 3,550K [92]. This results in substrate temperatures between 770K and 1470K. The growth area would be limited to the area heated by the flame, but methods to shift the flame, use multiple torches, or

use large, flat burners have been implemented with success [92, 97]. This results in an effective deposition area up to 5000 mm^2. CACVD has been found to work better than other CVD methods for growth metallic, titanium-based substrates [98], although such applications are rare. Advantages for CACVD include high linear growth rates and relatively lower cost, and disadvantages include high substrate temperatures and a lack of widespread adoption for the deposition process [92, 93].

2.3.2.3 Electromagnetically Excited CVD

CVD by means of electromagnetic excitation encompasses microwave plasma induced CVD (MPCVD), laser induced CVD (LIPCVD), and radio frequency induced CVD (RFCVD). Of all the CVD methods, MPCVD is the most widely used. Electromagnetic waves, typically around ~2.5 GHz for MPCVD, heat and ionize the gas molecules through various processes. Dielectric heating occurs as neutral, uncharged particles absorb energy from electromagnetic waves dependent on the wavelength and the resonance frequency of the of the gas molecules, with maximum energy absorption taking place when the two are equal [92, 93, 99]. When the energy density reaches a critical point, the gas becomes ionized [100]. Atoms can additionally be ionized through multiphoton absorption. This phenomenon happens when an electron enters a "virtual state" after absorbing one photon with an energy equal or higher to its energy bandgap and subsequently absorbs a second photon within a certain time period [101, 92]. After the gas transforms into plasma, further energy absorption takes place through free-free (also known as Inverse Bremsstrauhlung) absorption, ohmic heating, or stochastic heating. Free-free absorption is when electrons, induced to oscillate in the alternating electric field, absorb photons through collisions with charged particles [92]. Ohmic heating relies on collisions between electrons and other particles, similarly to free-free absorption, when a current is created through the conductive

plasma. Lastly, stochastic heating takes place at the interface between electron-less regions of plasma and the quasi-neutral regions, or areas with electrons. The oscillations in the interfaces between these regions, due to the changes in the current and electron field, further heat the electrons in the plasma [92, 93].

There are two types of plasma formations utilized in electromagnetic excitation induced CVD: plasma jets and plasma balls. In plasma jet systems, gas is funneled into a nozzle or tube. While contained, gas transforms into plasma when subjected to microwaves, radio waves, or a focused laser. Plasma proceeds to shoot out as a jet onto the substrate. Four notable plasma jet systems are the Torche à Injection Axial (TIA) plasma jet [102], Microwave Plasma Torch (MPT) [92], Inductive Coupled Plasma (ICP) plasma jet [103], and Laser Induced Plasma (LIP) plasma jet [104], which use microwaves, microwaves, radio waves, and lasers, respectively, as the excitation source. Plasma jet systems are relatively costly in power and material usage, but high growth rates can be achieved [92]. Plasma ball systems utilize a standing wave and careful process parameters to maintain a plasma ball over the substrate. Small changes in the absorption coefficient of the gas, penetration depth of the wave, or gas pressure will result in improper plasma formation, incomplete plasma formation, or poor growth [92, 93]. However, plasma balls provide better homogeneity in comparison to plasma jets. Three notable plasma ball systems are the Tubular Reactor (TR) [105], the Circumferential Antennae Plasma (CAP) system [106], and the Bell-Jar reactor [92]. Overall, plasma ball systems allow for very large deposition areas and high-quality diamond growth, but the chamber greatly influences process parameters and growth rates are relatively low. Diamond nucleation and growth using plasma for different substrate surfaces and for different lattice orientations is a well-researched and actively studied field [99].

2.3.2.4 Electrically Induced CVD

Finally, electrically induced CVD uses a direct current-generated plasma. Through a known current-voltage relationship, voltage is increased until current reaches glow discharge and arc discharge regimes [92]. Glow discharge ionizes gas and can form a plasma region over the region of the electrode; this regime is used for uniform deposition over large areas under low pressures. It is relatively simple and less costly; however, growth rates are low. After the current reaches a critical point as voltage increases, the electrode temperature rises to a point where electrons pass through thermal emission [92]. This arc discharge region requires lower voltages and power up to 100 kW, and the resulting plasma core is used for diamond deposition. Deposition using arc discharge allows for the highest documented growth rates (930 μm/hr) [107], although the arcs between electrodes are often unstable and undesired. Methods to stabilize arc discharge use plasma torches [108] and external magnetic fields [109].

The various CVD process parameters affect diamond formation and growth on the substrate. These include gas composition, pressure, temperature, and time. Furthermore, diamond type, size, and doping also depend on the parameters and type of CVD implementation. Typically, the deposition rate increases with increasing gas flow and power [92]. Pressure is also CVD type dependent, but the upper limit is 1 atmosphere due to the risk of explosion considering the gas chemistry. Overall, CVD from electromagnetic excitation is the most used technology for its favorable growth rates, deposition control, availability in power supply, and deposition area.

2.3.3 Homoepitaxial Growth

Homoepitaxial growth is diamond nucleation and growth on an existing diamond substrate – either HPHT or CVD diamond. Diamond is laser cut for a particular crystal orientation from an existing diamond source. The preferred diamond orientation for CVD is (100) for its growth stability and low defect potential (75, 109). Substrate surfaces are prepared through an oxygen-hydrogen plasma etch [75, 82, 92] as well as chemo-mechanical polishing or reactive ion etching [75, 111-113] for low surface defects and roughness. This limits dislocations during growth and leads to better diamond morphologies. Specifically on (111) oriented diamond, a scaife technique [114 – 115], chemical agents [75], and/or UV treatment [116] is required due to the particularly high hardness of the (111) orientation [75]. High single crystal growth rates upwards of 165 μmh^{-1} have been achieved on (100) diamond [107]. Large diamond plates that extend to twice the initial seed area have also been realized by optimizing the substrate holder for lateral growth [110, 117, 118]. Very high-quality single crystal diamond plates have been grown at a rate of 4 μmh^{-1} after adequate substrate preparation and optimization of MPCVD process parameters [119]. Additionally, CVD diamond growth in a UHV system with a 2% oxygen concentration and a 10% methane concentration has previously been reported to have nitrogen concentrations as low as 79 ppt [75].

2.3.4 Heteroepitaxial Growth

Heteroepitaxy involves the use of non-diamond substrates for nucleation and growth. This allows for larger growth areas, potentially cheaper substrate material, increased geometry variance, and compatibility with non-carbon materials. An interesting example of heteroepitaxy application is the creation of a 3D diamond network in a composite heat sink [120]. The challenges of heteroepitaxy are mismatches in coefficients of thermal expansion and lattice

constants, which lead to delamination and significant defect densities. Notable substrates used for heteroepitaxial growth include iridium, silicon carbide, and ruthenium. Dislocation densities of resulting diamond films or plates range from 10^{10} to 10^{5} cm^{-2} [75, 121]. To increase nucleation density and promote better lateral growth, seeding techniques are employed. These include electrostatic seeding, bias-enhanced nucleation, chemical nucleation, and nucleation though surface damage [122].

Iridium is currently the best substrate material for heteroepitaxial growth due to its lattice constant being only 0.028 nm different from that of diamond [123]. However, due to its high cost, thin films of iridium are utilized as the substrate material, and silicon is chosen as the bulk underlying material for its availability and better thermal expansion compatibility with diamond. Typically, films of $SrTiO_3$ or YSZ are sandwiched between layers of silicon and iridium due to the chemical incompatibility between iridium and silicon [75]. Much research has gone into using silicon or silicon carbide as the direct substrate for heteroepitaxy for its lower cost and better compatibility with electronic systems. (001) diamond growth on (001) silicon is achieved through successive stages of preferential growth in the <001> direction followed by growth in the <111> direction [75]. This allows more lateral growth from nucleation sites for film development as well as the flattening of misoriented diamond. However, for silicon, large lattice mismatch leads to non-uniform and mis-orientated diamond growth [124]. For better facilitation of heteroepitaxial growth, silicon carbide, or a thin layer of 3C-SiC, is used due to a decrease in lattice mismatch [75, 125, 126]. Increased oxygen concentration during CVD processes has been found to improve the quality of diamond grown on 3C-SiC due to its ability to effectively etch undesired carbonaceous material [75]. Lastly, heteroepitaxial growth on ruthenium films has

recently been shown to produce large, high quality (111) diamond [127], demonstrating the potential for a less costly alternative to iridium films.

Heteroepitaxial growth results in significantly higher defect density compared to homoepitaxial growth: the lowest achieved dislocation density for heteroepitaxial growth is on the order of 10^5 cm^{-2} [l21] while areas of homoepitaxially grown diamond have been made defect free [75, 128]. Due to the reliance of nucleation sites, diamond crystals grow laterally into each other to become a cohesive film. In doing so, a single crystal, sometimes multiple larger crystals, form with many defects. The different types of defects are well studied [129]. Increasing oxygen concentration during CVD [75], increasing diamond film thickness [130], and reducing stresses [131] are some methods that can reduce dislocation density.

Seeding techniques that introduce diamonds or other carbon materials onto the substrate surface include electrostatic seeding (nanodiamonds), chemical nucleation (diamondoids), and interlayer driven nucleation (diamond-like carbon, carbides, or carbide-forming materials) [122]. More interestingly, bias-enhanced nucleation and nucleation through surface damage are both methods that promote higher nucleation densities on non-carbon substrates. Bias-enhanced nucleation is the incorporation of a grounded tantalum rod ~4 cm while a voltage is applied to the substrate before CVD [122]. With low bias voltage (<-70 V), an ion shower occurs in the form of ion bombardment of the substrate. As a result, nucleation sites and non-diamond carbon form at the surface. High energy hydrogen radicals as well as oxygen etch away undesired carbon material. Nucleation densities upwards of 10^{11} cm^{-2} have been achieved by optimizing bias voltage and CVD process parameters [75, 132, 133]. Only some materials, such as silicon and iridium, may be used for bias enhanced CVD due to the requirements for the substrate to be conductive, be able to form carbide layers, and other characteristics that are generally not well

understood [132]. On the other hand, scratching or other damage of the substrate surface has been shown to improve nucleation density with varying success [122]. One study in particular has demonstrated highly ordered nucleation and high-quality diamond growth using ion beam etching [134].

2.3.5 Doping

The incorporation of dopants into the diamond lattice allows diamond surfaces to become conductive. High concentrations of impurities in the diamond lattice formed by substitutional atoms increase charge carrier concentration and shorten the high original bandgap of the 5.47 eV [82]. Resistivity of doped diamond films decreases with increasing dopant concentration, especially as the conductivity becomes governed by hopping conduction rather than band conduction at dopant concentrations over 10^{19} cm^{-3} [135]. Additionally, a nonlinear or bilinear relationship has been found between resistivity and temperature for doped diamond. The most effective method of doping is direct incorporation into the diamond lattice during CVD, but ion implantation and laser-facilitated doping can also be employed after deposition.

Boron is the best element to create p-type diamond due to its relatively low ionization energy (0.37 eV) compared to alternatives such as nitrogen (1.7 eV) [82]. Boron-containing compounds, such as diborane, trimethylboron, or triethylbore, are injected into the reactors to act as boron sources during deposition [135]. During MPCVD, boron radicals within the plasma etch the carbon surface during growth, leading to an inverse relationship between growth rate and boron concentration; on the other hand, boron heated during HFCVD is more stable and growth rates increase with higher concentrations [75, 136]. Boron concentrations exceeding 10^{21} with resistivities of ~5 mΩcm have currently been achieved [137]. Another notable form of p-type diamond is the lowering of sheet resistivity of diamond surfaces after hydrogen termination

[138]. Conversely, with an ionization energy of 0.6 eV, phosphorus has been the primary dopant of interest for creating n-type diamond [139]. Similar to p-type doping, during n-type doping, a phosphorous source, such as phosphine, is added into the reactor during deposition. Unlike boron, though, phosphorous does not face the same issues with etching carbon in plasma [75]. Dopant concentrations that have been achieved in n-type diamond are much lower than that of p-type diamond, with the highest concentrations being only on the order of 10^{19} cm^{-3}.

In addition to doping during CVD, dopants can be introduced through ion implantation. By bombarding diamond surfaces with high energy boron ions, the diamond lattice can be forcefully restructured to incorporate the dopant species. The ability for spatially selective doping and good doping control makes this method interesting for electronics manufacturing. However, two important issues arise regarding this. First, ion bombardment on the order of ~keV influence sp^3 carbon bonds to irreversibly transform into sp^2 after subsequent annealing [140]. In other words, the surface easily graphitizes at lower annealing temperatures after ion implantation. Residual surface damage other than graphitization is also present [75]. Methods to avoid this issue include rapid annealing after ion implantation to heal defects [141], ion implantation at ~MeV energy to burry ions deeper into the surface [75, 142], and etching of graphitic surface after ~keV ion implantation to reveal highly concentrated p-doped diamond [75]. Regions of diamond where dopant concentrations as high as 10^{21} cm^{-3} have been achieved through ion implantation [75, 143]. The second issue is the current inability to create n-type diamond [75]. A recently developed alternative method to dope diamond surfaces with phosphorus after deposition has been developed through use of a UV laser. This new method excites phosphoric acid on diamond using a 193 nm laser [144], and a resulting concentration of 10^{19} cm^{-3} was measured.

2.3.6 Growth of Large Crystals

Homoepitaxial and heteroepitaxial growth concepts can be scaled and repeated, to a point, to grow large crystals. For large 2D crystals, diamond wafers of up to 90 mm in diameter have been created through heteroepitaxial growth on iridium [145]. Alternatively, large, tight arrays of diamond seeds can allow a single "mosaic" homoepitaxial film, currently up to an area of 40 mm x 20 mm [82], to be created. For large 3D crystals, repeated CVD processes can produce crystals up to 17 mm tall [75], and crystals can be rotated after an initial growth phase for subsequent CVD diamond growth on different faces [146].

2.4 Electronics Applications

2.4.1 Overview

Efforts to increase processability and compatibility with existing technologies have resulted in use of diamond substrates, heat spreaders, and simple electronic devices. Commercial diamond substrates and heat spreaders are becoming more accessible. The mechanical strength and thermal conductivity of diamond are extraordinarily high, so it may be preferable to conventional materials in unique cases. On the other hand, the high thermal stability and bandgap makes diamond a material of choice for extreme high temperature and power electronics applications. Owing to doping technology and the additive nature of CVD, diamond devices can be formed in a similar fashion to conventional electronics. Some diamond-based electronic devices manufactured and tested in literature are discussed here.

2.4.2 Schottky Diodes

Diamond Schottky diodes are simple devices that have been successfully fabricated and tested. The potential for good electrical conductivity as well as high electrical breakdown field and high thermal conductivity make diamond an ideal material for Schottky diodes. Tungsten, nickel, and zirconium [147, 148, 149] demonstrate favorable Schottky contacts with diamond and are applicable at very high temperatures. One study investigated a vertically stacked Schottky diode, comprised of boron-doped diamond, doped silicon, nitrogen-rich Si: W alloy, and gold layers, and demonstrated successful functioning and a rectification ratio of ~10 at 1,000°C [147]. Other diamond-based Schottky diode configurations tested well at 400°C [150] and 450°C [149].

2.4.3 Transistors

Diamond transistors, including metal-semiconductor field effect transistors (MESFETs), junction field effect transistors (JFETs), metal/oxide/semiconductor field effect transistors (MOSFETs), metal insulator semiconductor field effect transistors (MISFETs), and bipolar junction transistors (BJTs), are a focus of study due to their high potential in power electronics. Often for 2D designs, doping by means of hydrogen termination of the surface is preferred; current densities and transconductance in transistors using hydrogen termination is comparable to those of transistors made with other semiconductors [151]. To maintain surface integrity, a passivation layer of Al_2O_3 deposited at 450°C protects the hydrogen termination and has helped diamond MOSFETs to operate at 400°C under 500V [152]. Other examples of diamond transistors operating at very high temperatures are boron-doped diamond MESFETs [153] operating at 350°C and JFETs [154] operating at 500°C.

2.5 Conclusion

Current manufacturing techniques and diamond device technology have been discussed. HPHT diamond is grown at relatively fast rates, and these methods are the most used for creating bulk diamond. Conversely, CVD processes are utilized for wafer production and device fabrication. Diodes and transistors have proven success in testing at temperatures (>400°C) significantly higher than ordinary electronics. CVD technology is a mature and ever-improving field. However, the fundamental requirements of extremely high process temperatures (>1,000°C), high material and system costs, and often relatively small deposition area imposes heavy limitations on adoption and compatibility with other materials. As a result, alternative, new methods of synthesizing diamond warrant further investigation and have potential to help adopt diamond as a more useful and applicable material in electronics.

3. Chapter 3: Experimenting with an Alternative Additive Method of Manufacturing Carbon-based Electronics

3.1 Introduction

3.1.1 An Alternative Method of Manufacturing Diamond Substrates

Polymer precursors present themselves as an alternative to CVD processes. Poly(hydridocarbyne) (PHC) and poly(naphthalene-co-hydridocarbyne) (PNHC) are carbon-based random network polymers that can be spin coated and pyrolyzed into diamond films. The synthesis and pyrolysis of these polymer has been reported with varying degrees of success [155-160]. Several methods have been developed for the synthesis of the polymer precursor, PHC. Early research references use of a sodium potassium alloy, which has been noted to be explosive in handled incorrectly [155-156]. A more popular method of producing PHC incorporates electrochemical reaction with chloroform [157-159, 161]; however, this results in the formation of chlorine gas. One safer method synthesizing the polymer requires a costly ball milling process to catalyze the reaction [160]. An alternative, closely related material, PNHC, has also been developed and is synthesized through a series of relatively safer chemical reactions.

These precursors are usually dissolved in THF and spun coat to a thickness of about 1 μm. After heating to 1,000°C in an inert atmosphere for 24 hours, PHC or PNHC sheds itself of a significant amount of its hydrogen and the carbon bonds reform to create the sp^3 bonds found in diamond. After pyrolysis, the resulting material is analyzed through Raman spectroscopy to confirm diamond presence.

3.1.2 Ohmic Contacts

Metallic ohmic contacts to electrically conductive diamond allow diamond-based components to interface with other systems. These ohmic contacts to diamond have been well researched over multiple decades. Titanium produces the best physical and electrical contacts to diamond of any metal due to the formation of titanium carbide layers at the carbon-metal interface [162-167]. Titanium is layered on diamond though sputtering or a thermal evaporative process. Annealing at or over 600°C for 6-30 minutes in an inert atmosphere produces the good contacts with diamond. Alternatively, heating using a pulsed laser with a wavelength of 248 nm also produces good contacts [167]. Hot-forging at over 1,000°C in an argon atmosphere for 1.5 minutes has been shown to create titanium-carbide contacts as well [168]. However, electrically conductive carbon contacts may interestingly demonstrate superior characteristics compared to metal contacts. Graphite grown on the surface of doped diamond exhibits an order of magnitude less contact resistance and improved linearity of between current and voltage compared to titanium-based electrodes [169].

3.1.3 Creating Conductive Surfaces on Diamond

The graphitization of the diamond occurs after thermally annealing above 1,000°C at loosely-understood, varying rates [170]. Catalysts for this transformation include iron, nickel, and copper. These metals dissolve the carbon bonds in diamond, allowing graphene sheets to grow within the carbon matrix. Iron, primarily studied due to the abrasion on diamond saws, reduces the activation energy for this transformation from 356 kJ/mol to 120 kJ/mol [171]. Using iron as a catalyst, single layer graphene has previously been reported after annealing iron on diamond to 785°C in vacuum [172]. Single layer graphene is preferable to multilayer graphene due to the orientations of carbon bonds in the material. The two dimensionality of graphene

results in superior properties in plane and less desirable properties out of plane. Increasing layers of graphene leads to decreased shear strengths and risks of layer discontinuity. Taking advantage of the diamond lattice orientation, vertical layers of graphene, normal to the diamond surface, have also been grown using iron [173]. Nickel catalyzes graphitization much faster. The transformation begins at 500°C on nanocrystalline diamond and graphite will dominate the diamond surface above 700°C [174]. Since nickel rapidly dissolves through the diamond surface, studies have optimized rapid thermal annealing procedures for single crystal (100) and (111) diamond [175-176] and ultra-nanocrystalline diamond [177]. Unlike iron and nickel, copper possesses self-limiting abilities to catalyze graphitization. This has made copper popular for growing monolayer graphene directly on copper through CVD. Research transforming diamond surfaces into graphene using copper is limited; however, one study finds monolayer graphene preferentially grows at 950°C when annealed between 60 to 90 minutes [178].

It is not uncommon for graphite to serve as electrodes in conventional electronics. Graphite and graphene are the most electrically and thermomechanically compatible with diamond as electrical contacts. Producing electronic devices almost entirely out of diamond and graphene theoretically provides an avenue for electronics viable up to 600°C in air. As of now, current academic findings support the theoretical manufacturing of all carbon electronics, with some experimental success [177]. However, different methods for the metal catalyzation of graphite and graphene have never been performed on the same diamond substrate, so electrical characteristics of the resulting surfaces have never been equally compared before. In addition, some processing details for metal catalyzation and the pyrolysis of polymer precursor are absent in the literature. The goal of this research is to assess the feasibility of producing all carbon

electronics using these two concepts. Details of PHC synthesis and post-processing as well as attempts to graphitize diamond using nickel, iron, and copper are presented.

3.2 Methods

The method of choice to synthesize is to pyrolyze the diamond polymer precursor PNHC. The reaction for synthesis primarily involves mixing sodium, naphthalene, and bromoform dissolved in tetrahydrofuran (THF) under a nitrogen atmosphere. This is detailed in two studies [156, 160], and the synthesis performed in this research follows the procedures outlined in the more recent study. The exact times and quantities of materials from the study are utilized, but some steps are altered for better compatibility with available equipment. Due to deviations in the synthesis procedure from the reference study, PNHC has been custom ordered from National Polymer for a quality comparison. This PNHC is synthesized using the exact procedure from the literature. Spin coating PNHC and baking the polymer to 1,000°C for 24 hours leads to diamond crystallization. This annealing procedure is attempted with both a tube furnace under nitrogen flow and a box sintering furnace under vacuum.

Two detailed methods of producing graphene and two methods of producing graphite have been chosen from the literature for reproduction. Depositing 50 nm of nickel onto single crystal or ultrananocrystalline diamond followed by rapid thermal annealing (RTA) at 800°C for one minute in an inert atmosphere has been documented to grow monolayer, bilayer, and multilayer graphene on the diamond surface [175-177]. Annealing a 20 nm thick nickel layer on nanocrystalline diamond at 800°C for at least 20 minutes will result in appreciable graphite formation [174]. Regarding iron, 40 nm of iron on single crystal diamond heated at 1150°C in vacuum for 15 minutes transforms the diamond into graphite [173]. Finally, one study finds that annealing copper on diamond only between 900°C and 1000°C allows for graphitization of

diamond [178]. The study of interest notes that an annealing time of 90 minutes is optimal for growing monolayer graphene. Most studies clean the diamond surface in a boiling acid bath. It is found in this study that this step is unnecessary. Using these methods, graphene and graphite growth is attempted on diamond of the same type and roughness. Unfortunately, complications related to the annealing process have prevented graphitization from being analyzed for all cases, except for RTA of nickel for monolayer growth. Hole mobility and sheet concentrations are documented. The diamond films formed from pyrolysis of PHC or PNHC in literature have been reported to be polycrystalline [155] or nanocrystalline [156-158, 160]. Therefore, ultra-nanocrystalline and polycrystalline diamond substrates are used in this study.

3.3 Experimental

3.3.1 Equipment and Materials for PNHC Synthesis

The equipment used for PNCH synthesis were a Schlenk line, a fume hood, one 1 liter 3 neck round bottom flask (3NRBF), one 500 mL 3NRBF, a distillation head, a 250 mL separation funnel, three 20 gauge cannulas, a 200 mL Buchner funnel, a 1 liter vacuum Erlenmeyer flask, a 250 mL addition funnel, a reflux condenser, a cryotrap filled with liquid nitrogen, glass stoppers, septa, a heat gun, a hot plate with magnetic stirring capability, and a vacuum pump. The materials for PNCH synthesis were procured from Sigma Aldrich. The sodium, bromoform, and THF were obtained anhydrous and inhibitor-free, when applicable. High purity nitrogen gas was used.

3.3.2 Preparation

Before the reaction, THF was dried using a sodium benzophenone ketyl and extracted through distillation. Glassware was first dried in a vacuum oven. Nitrogen and vacuum lines then connected the two 3NRBF. Vacuum was pulled from the flasks, and a heat gun was used to heat the flasks for 3 minutes to evaporate off remaining water on the glass surface. While sealed with glass stoppers and septa, nitrogen purging and subsequent vacuuming of the flasks were performed three times to eliminate atmospheric contaminants. 5 grams of benzophenone was measured and inserted into the 1 liter 3NRBF. Under high nitrogen pressure, the benzophenone was quickly dropped into the flask after a glass stopper was briefly removed from one neck. Three more cycles of nitrogen purge and vacuum followed to eliminate any atmospheric contamination that may have occurred after this maneuver.

Next, cannulas connected the container of THF and the 1 liter 3NRBF through puncturing of septum. A nitrogen line was inserted into the THF container while a needle punctured a septum in the flask to allow the pressure to vent. THF in the container was displaced and traveled to the flask through the cannulas. Once the 1 liter 3NRBF was about halfway filled, this procedure was terminated. Afterwards, 3 grams of sodium were measured using a beaker of mineral oil. The sodium was procured in the form of chunks. As a result, the oxide layers of these chunks were carefully scraped off, and the chunks were chopped into smaller pieces. These pieces were quickly inserted into the flask under high pressure. A reflux condenser was purged with nitrogen for about 15 minutes and quickly placed onto the middle neck of the 3NRBF.

The flask was placed into a mineral oil bath on a hot plate. The mixture was heated to 100°C and stirred at 250 rpm. The contents of the flask transformed into a blue mixture (Figure 1), followed by deep purple color, indicating the consumption of virtually all the water from the

THF. The reflux condenser was removed, and a distillation head connected the two 3NRBF. Once 300 mL was distilled off into the 500 mL 3NRBF (Figure 2), the procedure was terminated. The remaining mixture in the 1-liter 3NRBF was opened to atmosphere and quenched with isopropanol. In addition to drying the THF, the bromoform was also dried to ensure water elimination from the solution. A small Erlenmeyer flask filled with calcium chloride was purged with nitrogen. 8 mL of bromoform was placed into the flask for drying (Figure 3).

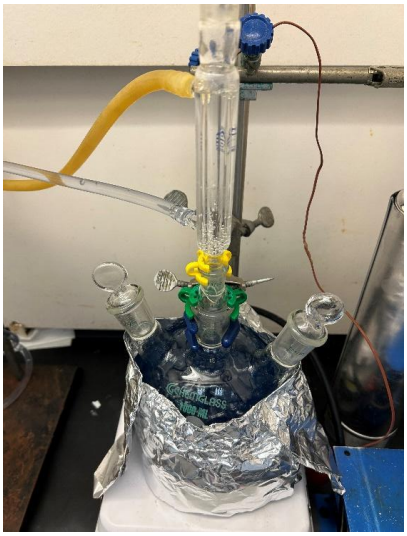

Figure 1: The mixture of sodium, THF, and benzophenone turned blue as the THF dried.

Figure 2: THF distilled into the 500 mL 3NRBF after the mixture turned dark purple.

Figure 3: Bromoform dried over calcium chloride while bring purged under nitrogen.

After the contents of the 1-liter 3NRBF were removed, the flask was cleaned and vacuum dried. The flask was connected to the Schlenk line as well as the 250 mL addition funnel. The same procedures mentioned above were used to create a dry, nitrogen rich environment. 40.23g of naphthalene was measured and quickly placed into flask under high pressure. The 3NBRF was again nitrogen purged and vacuumed 3 times. 250 mL of the dried THF was transferred from the 500 mL 3NRBF to the addition funnel using cannulas (Figure 4). Once measured in the addition funnel, the THF was dropped into the 1-liter 3NRBF. Then, 5.09g of sodium were cut, measured, and inserted into the flask under high pressure. The mixture was stirred at 300 rpm for 2 hours. The contents of the flask proceeded to turn dark green (Figure 5). 50 mL of the remaining dry THF was transferred to the addition funnel. 5.4 mL of the bromoform dried in the calcium chloride was extracted and placed into the addition funnel as well.

Figure 4: Dry THF transferred between flasks using cannulas and an addition funnel.

Figure 5: The solution of sodium, THF, and naphthalene turned dark green after mixing for two hours.

3.3.3 Primary Reaction

A -70°C bath was created by immersing dry ice into a pool of isopropanol. The 3NRBF containing the mixture was lowered into this bath. Once cooled, the bromoform/THF solution in the addition funnel was added dropwise over the duration of 15 minutes. The mixture was stirred at 300 rpm during this stage. Next, the mixture was removed from bath and allowed to be heated to room temperature. The contents of the flask were stirred at 500 rpm for 1 hour.

3.3.4 Work-Up

The solution was subsequently quenched with ice water. The liquid color turned light brown, and white salts were visually present in the solution. The vacuum Erlenmeyer flask, the Buchner funnel, and filter paper were used to separate the solution from the precipitated salts. The solution was then transferred to a one neck round bottom flask. A rotary evaporator was used to distill solvents off at a temperature of 65°C (Figure 6). The flask was then connected to a cryotrap immersed in liquid nitrogen as well as the vacuum pump. The remaining residue evaporated to dryness (Figure 7). Afterwards, 500 mL of hexane was heated on a hot plate set to 60°C.

Figure 6: A rotary evaporator quickened the removal of solvent due to liquid films evaporating at increased rates as the flask is rotated in a warm pool of water.

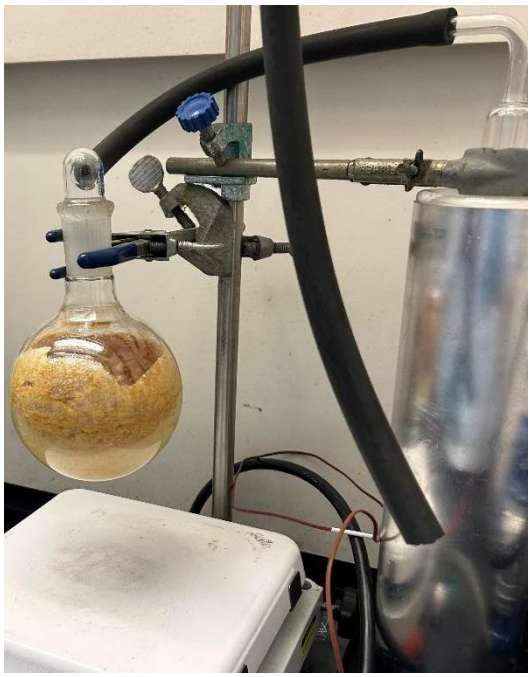

Figure 7: The solid residue was evaporated to dryness using a vacuum pump. A cryotrap froze solvents before reaching the pump.

In two separate maneuvers, 250 mL of hexane was used to wash the residue through the process of stirring, letting sit for a minute, and decantation. A solution of 1 mL concentrated HCl and 50 mL of distilled water was prepared and placed into the flask with the residue. 30 mL of chloroform was placed into the solution. The contents of the flask were placed into a separatory funnel. In two separate instances, the flask was rinsed with 25 mL of chloroform and the fluid was placed into the separatory funnel (Figure 8). The visually distinct bottom layer in the separatory funnel was extracted and placed back into the separatory funnel. Next, 50 mL of distilled water was added to the separatory funnel. The funnel was closed, turned upside down, and mixed. The gas in the funnel was vented between periods of mixing. Again, the bottom layer was extracted out. This action was performed twice.

Figure 8: The separatory funnel allowed for fluid extraction based on density differences.

Three scoops of calcium chloride were used to dry the chloroform in the solution. The calcium chloride was extracted using a vacuum Erlenmeyer flask, the Buchner funnel, and filter paper. 50 mL of distilled water was added to the solution and stirred. The vacuum pump

connected to the cryotrap was used to evaporate the contents of the flask to dryness. The solids in the flask were washed with 20 mL of dichloromethane and stirred. A rotary evaporator was used to reduce the resulting solution to 40 mL. Finally, 40 mL of hexane was added to the solution, and the final polymer was extracted using filter paper, the Buchner funnel, and the vacuum Erlenmeyer flask. This step initially yielded 0.194g of polymer. It was performed a second time to again yield another 0.277g of polymer. The polymer was in the form of a beige powder (Figure 9), which agreed with findings in literature [160]. GPC and NMR analysis on this powder has not been performed for identity and purity confirmation.

Figure 9: The beige polymer was collected on a plastic boat and weighed.

3.3.5 Spin Coating PNHC

All spun coat films were deposited on 1 cm x 1 cm silicon chips. The native oxide layer was etched in a 6:1 buffered oxide etching solution for 10 minutes and washed with distilled water.

The polymer was previously reported to be soluble in THF, and thin films were made using a solution of 0.2g/mL and spin coating at 1,000 rpm for 5 minutes [155]. Higher concentrations were used to determine the effect of PHNC concentration, if any, on resulting films. Dissolving PNHC in THF at a concentration of 0.4g/mL was attempted; however, upon

visual inspection, the solution initially appeared to be saturated, as a noticeable polymer precipitated. Attempts to spin coat this saturated polymer resulted in failure (Figures 10 and 11) to develop a thin, homogeneous film. A spin coating speed of 1,000 rpm and quantity of 40 µL was initially used. After 6 minutes of failing to develop a homogenous film, speeds of 2,000-4,000 rpm were used with no success.

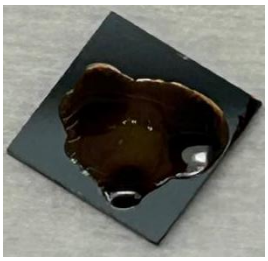

Figure 10: The fluid from the 0.4g/mL mixture spread limitedly after spin coating.

Figure 11: The film deposited from the 0.4g/mL mixture after baking at 80°C for 10 minutes.

A concentration of 0.33g/mL allowed for the better dissolving of PNHC (Figure 12). Solid particles were still separated from the solution. Spin coating 20 µL of this solution at a rate of 2,000 rpm for 2 minutes resulted in a flat, thin film (Figure 13). The film was baked at 80°C for 10 minutes to cure. The film thickness was measured to be 1.6 µm thick using a profilometer.

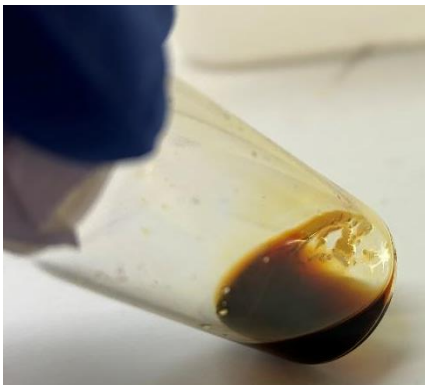

Figure 12: Solids not dissolved in the 0.33g/mL mixture after mixing and letting sit overnight.

0.1 mL of the concentrated solution was extracted to create a 0.2 g/mL solution following the addition of 0.065 mL of THF. Spin coating 20 µL of this solution at 1,000 rpm for 5 minutes, the process used with this concentration of precursor polymer in THF in a previous study [155], corresponded to a film with a thickness of 3 µm (Figure 13).

Figure 13: Polymer films created from 0.33g/mL, 0.4g/mL, and 0.2g/mL mixtures, presented from right to left.

After a week of storage, the 0.33g/mL solution matured into a homogenous liquid. What was an insoluble portion of polymer, which persisted over the duration of two days, completely dissolved into the THF. A film was spun coat using 40 µL of the solution at 3,000 rpm for 4 minutes and cured at 80°C for 10 minutes. The layer of polymer was non-uniform with a thickness ranging between <1 µm and 15 µm (Figure 14, left).

A 0.2g portion of the PNHC acquired from National Polymer was completely dissolved in 1 mL of THF. 40 µL of this solution was dropped on the silicon chip and spun at 1,000 rpm for 5 minutes (Figure 14). The film thickness was nonuniform and measured to be less than 15 µm.

Figure 14: Film deposition from the synthesized homogeneous 0.33g/mL solution (left) and the 0.2g/mL solution (right) created using the polymer obtained from National Polymer.

3.3.6 Pyrolysis of Polymer Films

The first spun coat films created from the 0.4g/mL, 0.33g/mL, and 0.2g/mL mixtures were first pyrolyzed using a tube furnace sealed with metal endcaps that contained narrow inlet and outlet ports (Figure 15). Nitrogen gas initially flowed through the furnace at a rate of 4.72 L/minute for the duration of the heating at 10°C/minute to 1,000°C. However, this flow rate was reduced to 1.89 L/minute to compensate for the rate of pressure loss in the gas cylinder. The films were baked for 24 hours and cooled naturally.

Figure 15: A tube furnace with metal endcaps was first used for long term pyrolysis.

The film created from the homogenous 0.33g/mL solution as well as a film spun coat from a 0.2g/mL solution of PNHC from National Polymer were pyrolyzed in a sealed sintering furnace pumped to a vacuum of ~10 kPa (Figure 16). After the furnace was heated to 1,000°C, the vacuum measured ~40 kPa.

Figure 16: A sintering furnace with metal endcaps was used for long term pyrolysis for the second batch of films.

3.3.7 Graphitization of Diamond

Four 10 mm x 10mm ultrananocrystalline diamond-on-silicon chips were initially procured from MTI Corporation. These substrates composed of a 2 μm thick layer of diamond grown on a 1 μm formed on top of a 500 μm thick layer of silicon. The diamond was stated to be "as grown," and the surface roughness was estimated to be <10 μm. Nondestructive AFM tapping was used to confirm this roughness (Figure 17).

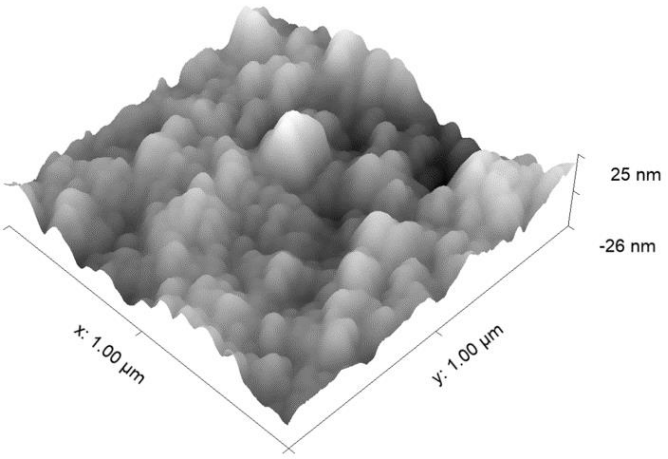

Figure 17: A roughness map of a 1 µm x 1 µm area was acquired after AFM tapping measurements.

Next, organic material was removed through UV/Ozone treatment for 10 minutes. For three of the four samples, potential graphitic or metallic contaminants of the diamond surface were removed by placing the material in a boiling acid bath of 3:1 sulfuric acid to nitric acid at 150°C for 15 minutes (Figure 18). The fourth sample could not be placed into the acid bath due to having remnants of thermal tape still applied on the silicon for the AFM measurements.

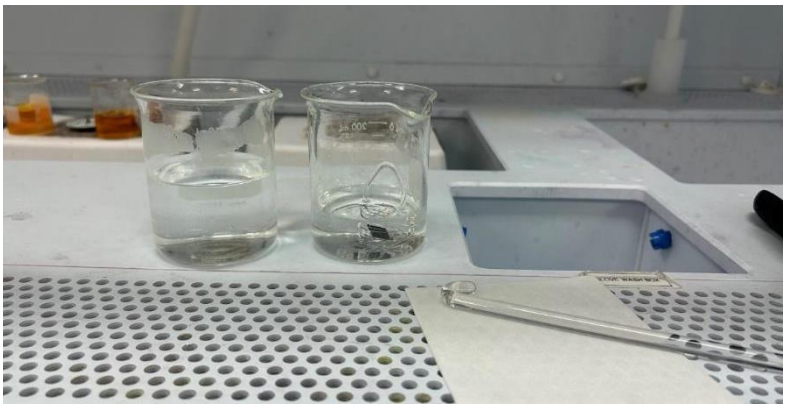

Figure 18: A glass bucket was used to immerse the diamond-on-silicon chips into the 3:1 sulfuric acid to nitric acid solution.

Directly after cleaning, nickel, copper, and iron were deposited using an ATC 1800 magnetron sputtering system at a vacuum of $7*10^{-7}$ torr. 20 nm of nickel, 50 nm of nickel, 40 nm of iron, and 200 nm of copper were deposited on different samples (Figure 19).

Figure 19: 50 nm of nickel (top left), 20 nm of nickel (top right), 40 nm of iron (bottom right), and 200 nm of copper sputtered onto diamond surfaces.

The metal on diamond was next annealed as consistent with previous studies. The annealing details are outlined in Table 4.

Sample	Ramp Rate	Annealing Temperature	Hold Time	Atmosphere
20 nm Nickel	4.3°C/minute	800°C	30 minutes	Nitrogen
50 nm Nickel	40°C/second	800°C	1 minute	Nitrogen
40 nm Iron	4.2°C/minute	1,000°C	15 minutes	Argon
200 nm Copper	5.3°C/minute	950°C	90 minutes	Argon

Table 4: The annealing parameters used previous studies were used in this research

Raman microscopy was performed using a 522 nm laser to characterize the surfaces of the diamond. Because nickel dissolves through the diamond and iron does not reflect the laser, no preparation was necessary to capture the Raman spectra of those diamond surface. The copper was removed from the substrate by placing the chip in a bath of 10% nitric acid. This removal process was reported to be benign to any underlying graphene material [179].

In addition to ultrananocrystalline diamond, five 10 mm x 10 mm polycrystalline diamond chips from Element Six were procured. The chips possessed a thickness of 0.5 mm and a polished surface with a roughness of 50 nm. The diamond chips were cleaned by rinsing in ethanol, acetone, and distilled water as well as 10 minutes in a UV/ozone treatment. The same metal depositions and annealing characteristics were performed on four of the five polycrystalline diamond chips. An additional RTA of the copper on diamond chip was performed with a ramp heating of 30°C/s to 950°C and held for one minute (Figure 21).

Figure 20: The first annealing tests were conducted for metal-on-diamond chips using this tube furnace at the Nanocenter.

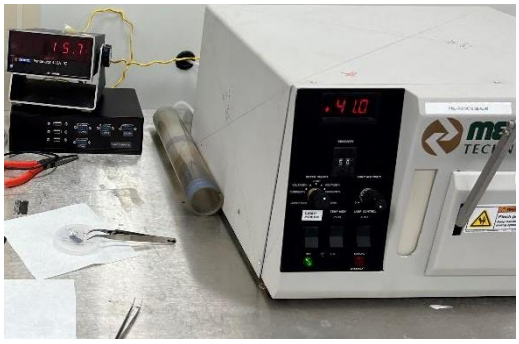

Figure 21: The RTA system at the Nanocenter was used for 50 nm nickel and copper samples.

3.4 Results and Discussion

3.4.1 Synthesis of PNHC

The procedure outlined in the literature provided little detail regarding the equipment, preparation, and workup of the synthesis. As a result, an expert at Exponent, a consulting firm, was brought in for advice in performing the synthesis. Another synthesis was performed as outlined in the experimental section beforehand with a few differences. One major alteration between the two synthesis was distilling solvent off using a distillation head instead of a rotary evaporator. The only distinction with utilizing a rotary evaporator was a reduction in time. A more important difference in the work up process of the first synthesis included an extra step of adding 300 mL of hexane after quenching the reaction with ice water. This step was necessary to extract the precipitated salts. The reason for the need for this step was undetermined. The preparation and reaction of the first and second synthesis procedures were performed the same way; therefore, it was not understood why hexane was needed to precipitate the salts in the first synthesis. Additionally, the second synthesis necessitated two stages for the final removal step of the polymer, where polymer was filtered using the Buchner funnel. The second stage was absent in the literature and the first synthesis. The reason for this deviation was believed to be the reduction of the solution after the addition of dichloromethane to 40 mL instead of 10 mL as stated in the literature. The first synthesis reduced the solution to 20 mL. Outside these differences, the reported quantities and color of the polymer and intermediary stages of the synthesis in literature agreed with those in the synthesis in this study. However, it cannot currently be demonstrated that the resulting polymer is PNHC without GPC analysis.

3.4.2 Spin Coating PNHC

The polymer was first partially dissolved in THF at a concentration of 0.4g/mL. The solution was visually saturated with additional polymer suspended in the THF and large pieces that remain separate from the THF. To preserve the polymer, high concentrations in THF were first tested. 0.4 µL of this solution was unable to be spun into a film. 200 µL of THF was added to this solution, resulting in a 0.33g/mL concentration. There was no visual suspension of the polymer, and the large pieces previously seen in the 0.4g/mL solution were still visible. In literature, it is not uncommon for some portion of the polymer to be insoluble or partially soluble [158, 180-181] after performing different methods of synthesis. The fluid portion of the 0.33g/mL mixture was 66% more concentrated and yielded a 60% thicker film compared to values in literature [152]. Next, using the same spin coating parameters given in a previous study [155], the 0.2 g/mL solution yielded a film three times thicker compared to the study and about twice as thick compared to using the 0.33g/mL mixture. Molecular weight differences or the inhomogeneity of the stock solution used to create the 0.2g/mL solution may be contributing factors to the larger thickness. Lastly, spin coating the completely homogenous 0.33g/mL solution resulted in a non-uniform film similar to, but much thinner than, the film created from the 0.4 g/mL mixture. To create more uniform films, 0.2 g/mL should be the highest concentration utilized in further testing.

3.4.3 Pyrolysis of PNHC Films

Pyrolysis using the tube furnace failed to yield diamond crystallization. The films on the silicon chips visibly whitened (Figure 22), and Raman spectra contained only peaks for silicon. Two experimental limitations may have prevented diamond formation. The end caps of the tube furnace would start flush with the heating tube; however, despite efforts to fasten them, limited load compressed these end caps to clamp them to the furnace. This led to the end caps shifting after heating to allow a small gap at the inlet and outlet (Figure 22). This issue was compounded with the limited available flow rate. The limited continuous flow rate of 1.89 L/min may have been insufficient to purge the large tube; despite the positive pressure, room air may have been able to enter and oxidize the films during baking.

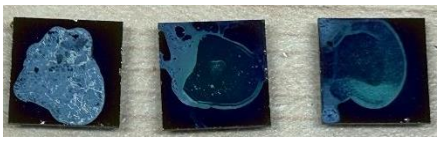

Figure 22: The first batch of polymer films degrading after annealing in the tube furnace.

Figure 23: A small gap between the endcaps and the tube furnace was present after pyrolysis.

Likewise, pyrolysis using the sealed sintering oven only degraded the polymer films instead of resulting in diamond crystallization for both the synthesized polymer and the acquired polymer from National Polymer. A vacuum of only ~10 kPa was achieved due to the limitations of the sintering furnace seal. It appears that the residual atmosphere, as well as any possible outgassing from the interior ceramic material, was able to react with the polymer film before diamond crystallization could begin.

3.4.4 Graphitization of Ultrananocrystalline Diamond

The attempt to catalyze the graphitization of ultrananocrystalline diamond was unsuccessful. First, Raman microscopy and AFM tapping was performed to characterize the quality of the diamond film. The Raman spectrum of the ultrananocrystalline diamond is shown in Figure 24. The gradual increase in signal intensity was a sign of surface fluorescence. This is not unusual and may be attributed to the presence of organic material prior to any cleaning. The approximate peaks of 1142 cm^{-1}, 1360 cm^{-1}, and 1520 cm^{-1} were present. The first peak is typical of nanocrystalline diamond [182], and the second peak, commonly known as the 'D' peak, is distinct to the sp^3 carbon bonds in diamond. Ultrananocrystalline diamond often exhibits a peak shifted slightly away from the G peak at 1560 cm^{-1}, which is characteristic to the sp^2 bonds in graphite. The third, much wider peak centered around 1520 cm^{-1}. The peaks exhibited from the diamond samples confirm that the material was ultrananocrystalline diamond. The widths of these peaks, however, were much wider than those shown in literature [182-183]. The surface roughness of the diamond film was estimated to be <10 nm. To confirm this, AFM tapping was used to map the roughness of the in a 1 µm x 1 µm area on the chip. The root mean square

roughness was confirmed to be 8.24 nm. Measurement of a larger, 20 µm x 20 µm area yielded a root mean square roughness of 8.72 nm.

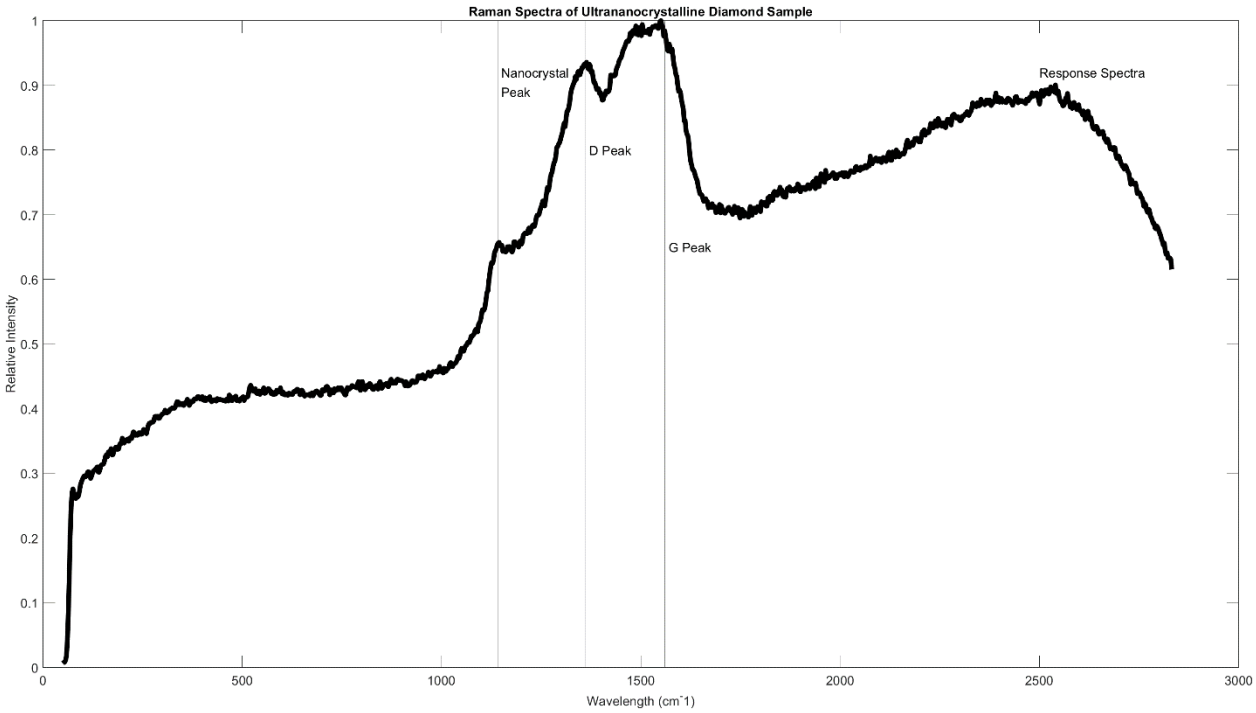

Figure 24: The Raman spectra of the ultrananocrystalline diamond and relevant carbon peaks confirm the identity of the procured material.

The metal deposition occurred using a magnetron sputtering system at a vacuum of $7*10^{-7}$ torr. The thickness of the metal films was not physically measured. Instead, each metal had a respective rate of deposition. Nickel and iron deposited onto the silicon oxide at a rate of approximately 100 angstroms per minute, and copper deposited at a rate of 160 angstroms per minute.

After thermal annealing, the Raman spectra of the surface was collected (Figure 25). For the samples with nickel and copper deposited, the Raman spectra was near identical to that of bare silicon. No carbon was shown on the surface of these samples. Regarding RTA of the 50 nm of nickel on diamond, a very thin film separated from the top surface of the chip. Raman spectra

of this film was identical to the surface beneath it. It is of interest to note that the sample with iron deposited on diamond demonstrated a slightly different Raman spectra, with carbon present. However, the only carbon response was a weak disordered carbon peak at 1294 cm^{-1}. Other peaks present lower than 500 cm^{-1} corresponded to iron oxide on surface. The weak carbon response likely resulted from underlying diamond layer oxidizing during the annealing process. This hypothesis is discussed further in the following section. Because the chip with iron deposited was the only sample not cleaned with a boiling acid bath, it can be reasonably concluded that the acid bath removed the diamond from the underlying silicon oxide layer. The hot acid bath was chosen as a cleaning method to create pristine surfaces with minimal external contaminants. Boiling acid treatment is a standard cleaning solution [184]; it is performed in most relevant studies for graphitization [175-179], and even with nanocrystalline diamond [185]. The wide peaks and fluorescence shown in the Raman spectra of the ultrananocrystalline diamond may be indicative of the presence of impurities that may have caused the diamond film to be removed in the presence of the boiling acid. Alternatively, ultrananocrystalline diamond may be fundamentally incompatible with this treatment, or the bonding between the diamond layer and the silicon oxide layer may have been susceptible to breaking in the presence of the acid.

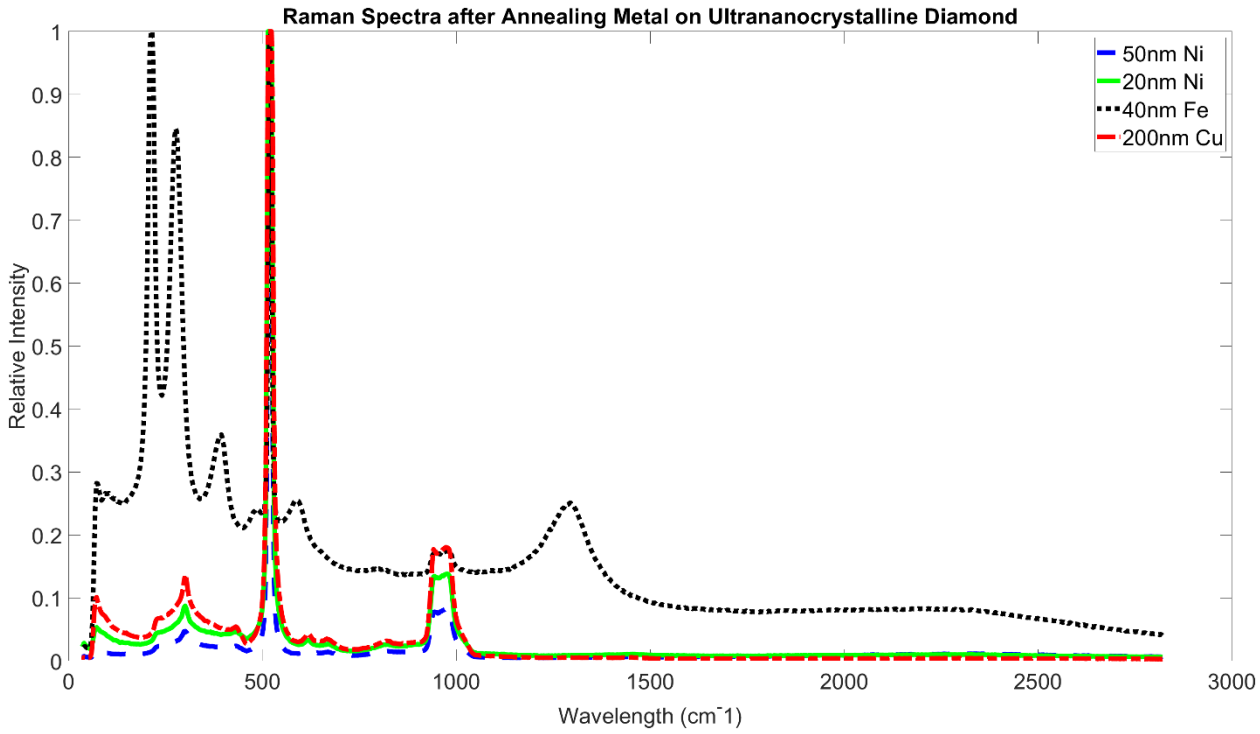

Figure 25: The Raman spectra of the chip substrate after annealing 200 nm copper, 20 nm nickel, 50 nm nickel, and 40 nm iron, plotted from bottom to top.

3.4.5 Graphitization of Polycrystalline Diamond

Raman spectroscopy was performed to characterize and confirm the identity of the polycrystalline diamond (Figure 26). The sharp, focused peak at the D peak demonstrated the material was pure diamond. Given the Raman spectra demonstrating very pure diamond, the boiling acid treatment was forgone for the polycrystalline diamond.

The RTA of nickel on diamond led to graphene growth on the diamond surface. The Raman spectra of the surface featured a prominent G peak at 1350 cm^{-1} and a 2D peak at 2686 cm^{-1} (Figure 27). The presence of both peaks indicated the presence of graphene layers, and the ratios of the intensities of these peaks can be used to estimate the number of graphene layers.

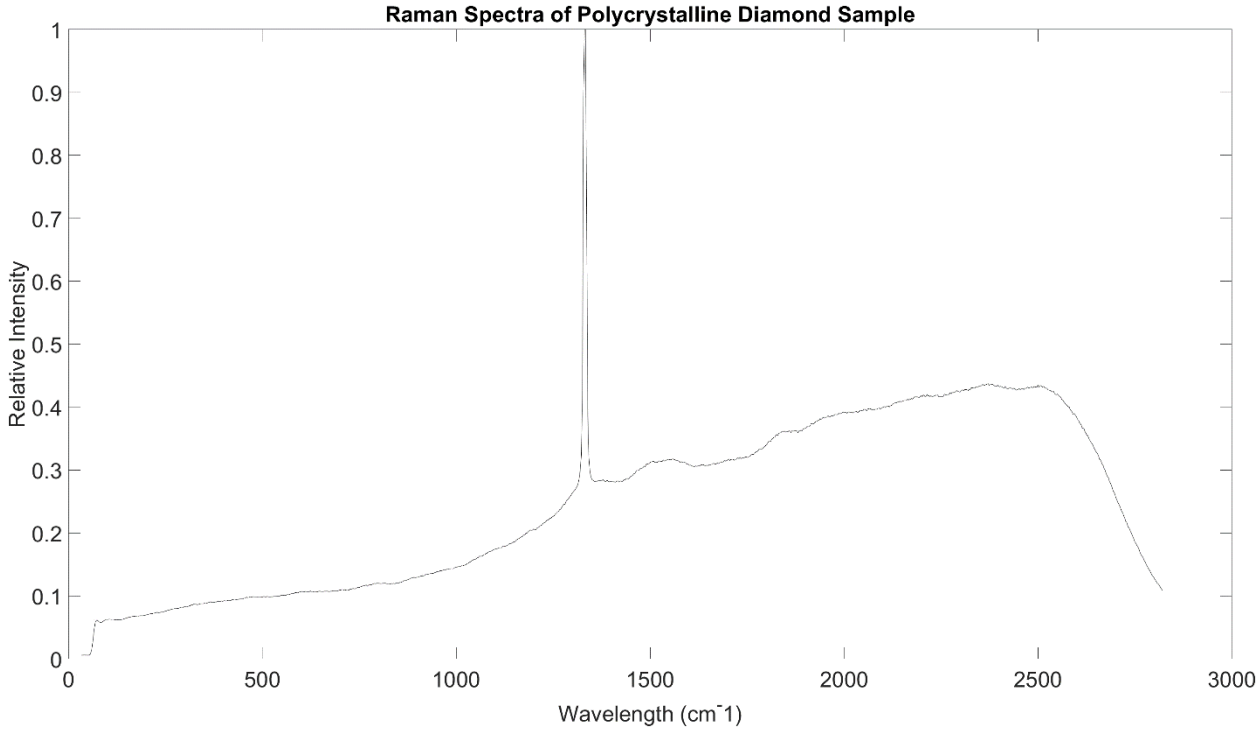

Figure 26: The Raman spectra of the polycrystalline diamond as received from Element Six

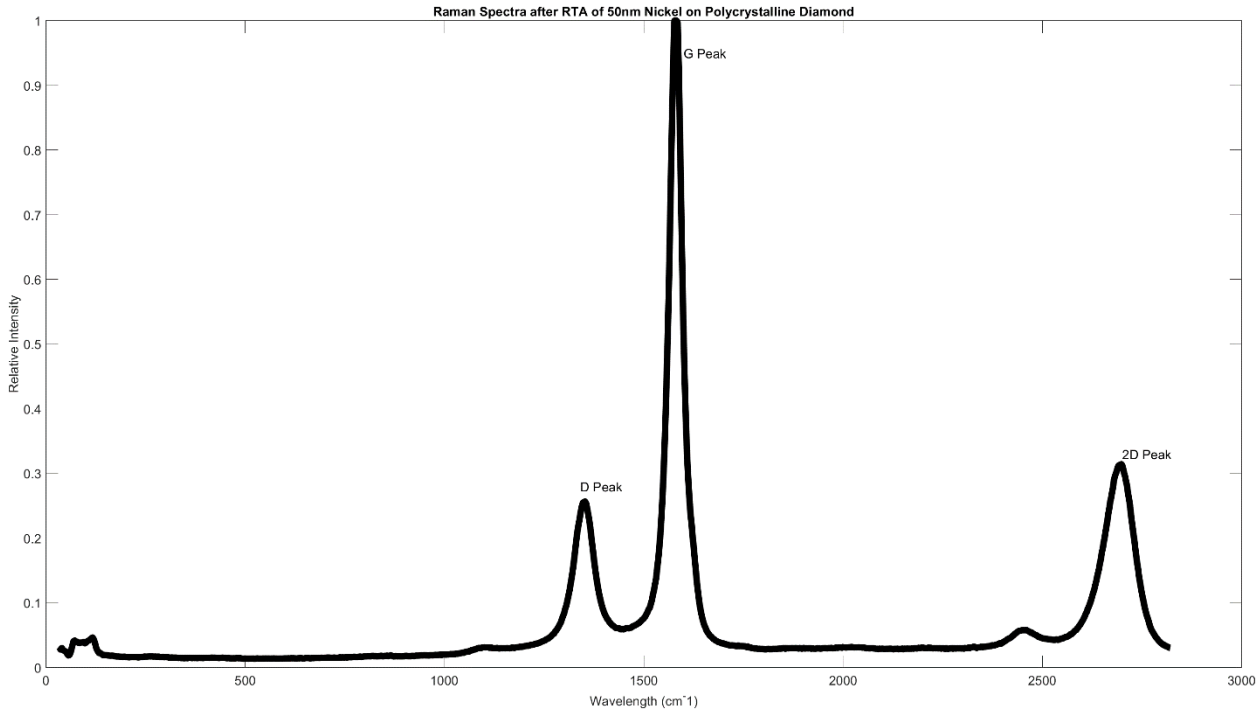

Figure 27: Raman spectra of the graphene surface after RTA of nickel on polycrystalline diamond after 1 minute at 800°C

It has been previously shown that the number of graphene layers grown by heating metal on diamond is nonuniform [175-178]. Therefore, 2D Raman mapping was performed after the confirmation of graphene growth. 2D Raman mapping measured the Raman spectra at different points in an array on a set area of the surface. A 90 µm x 90 µm area was sampled with a gap of 1 µm between measurements. Since the spot size of the laser was also approximately 1 µm, measuring the Raman spectra with this gap size effectively measured the Raman spectra of the entire area. According to relevant studies [175-176, 178], a G to 2D peak intensity ratio close to 0.5 demonstrates monolayer graphene. A ratio close to unity shows bilayer graphene, and a ratio greater than 2 exhibits 3 or more layers of graphene. The results of the 2D Raman mapping demonstrated that the entirety of the sampled area consists of multilayered graphene. The increased roughness of the diamond used in this study may have contributed to the growth of more graphene layers compared to the findings of studies that followed a similar procedure. This conclusion is supported by findings comparing graphene growth over smooth diamond and over stepped, jagged diamond surfaces [176].

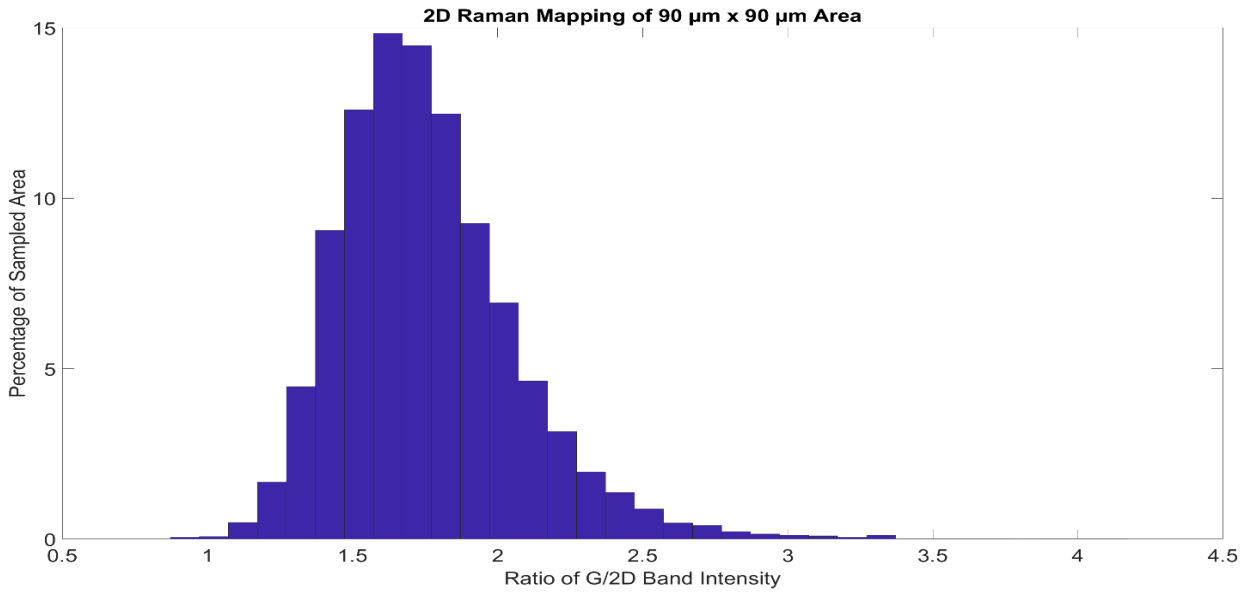

Figure 28: Frequency histogram of the ratio of the G peak and 2D peak intensities of the graphene grown from RTA of nickel on diamond

The sheet concentration and mobility of the graphene film were measured using an Ecopia HMS-500 Hall Effect Measurement system. The loading mechanism used 4 indium pins clamped at each corner of the sample. Measurements were taken at room temperature and under a magnetic field of 0.51 Tesla. The sheet carrier concentration and mobility were found to be $1.0*10^{15}$ cm^{-2} and 629.1 cm^2 Vs^{-1}. Electrical conductivity is proportional to the product of these two values. The sheet concentration and mobility were exceptionally high compared to previously reported values, the highest being $5.7*10^{13}$ cm^{-2} [176] and 410 cm^2 Vs^{-1} [178], respectfully. The differences in this research and what was reported in literature may be a few reasons for these improved electrical properties. The diamond material was cleaned using a boiling acid bath in each of these studies. The use of oxidizing acids resulted in an oxygen-terminated surface prior to metal deposition. The previously tested diamond was also exceptionally smooth, each having a root mean square roughness of less than 5 nm. Lastly, the method of metal deposition utilized in all the previous studies was electron-beam evaporation. Although specifically untested between nickel and diamond, sputtering generally results in improved interface adhesion compared to evaporative techniques.

Unfortunately, long term annealing of metal films on diamond faced process complications and ultimately failure. First, 20nm of nickel was annealed at 800°C for 30 minutes. Raman spectra of the surface consisted of neither the G nor 2D peak (Figure 29). The surface was also non-conductive. Initially, it was not understood why no graphite or graphene layering was present. However, after the iron was annealed on diamond at 1,000°C for 15 minutes, the reason was clear. After the annealing process, the diamond material entirely burned up. Nitrogen was used for the inert atmosphere; however, it is clear that oxygen was present in the furnace during the annealing process. With exception of a narrow outlet, the tube furnace was

sealed during heating; therefore, it is thought that the oxygen that entered the furnace upon loading of the sample was not displaced before heating to the critical temperature of burning. The nitrogen flow rate was only 30 mL/minute, so it is likely this displacement did not occur.

Considering this issue, an RTA test was first tested with the copper on diamond sample. The RTA of nickel on diamond did not have similar issue, likely due to the smaller furnace size relative to the flow rate (10 liters per minute) and the lower duration under high temperatures. Additionally, although not discussed, annealing copper on diamond at 950°C for a short duration was shown to produce bilayer graphene [178]. However, the exact heating period was not given. The RTA system could only support heating at 950°C for one minute, so an RTA of test of copper on diamond was first performed before attempting long term annealing. After the RTA, the sample was immersed in a 100 mL solution of 10% nitric acid. The acid solution etched copper off completely after 1 hour. The resulting surface was featureless and non-conducting, indicating a failure of graphitization. The cleaning and copper deposition was repeated. Before long term heating, the furnace was purged for 6 hours. The sample again burned up, demonstrating an issue with the inert gas flow rate.

In an effort to reproduce another method of graphitization, cleaning, iron deposition, and annealing was performed on the fifth diamond chip. A new environment was used to eliminate avenues of diamond oxidation. A sealed sintering furnace from Sapphire and argon gas were employed to improve the inert atmosphere during heating. The furnace was purged for half an hour before heating. Instead of completely burning, this annealing process visibly deformed and thinned the diamond chip. Similar to the long term annealing of nickel on diamond, the Raman analysis of the surface indicated no presence of graphite (Figure 29). The lack of graphite on

these surfaces is much more likely to be the result of oxidation rather than an incompatibility with the annealing process and the diamond material.

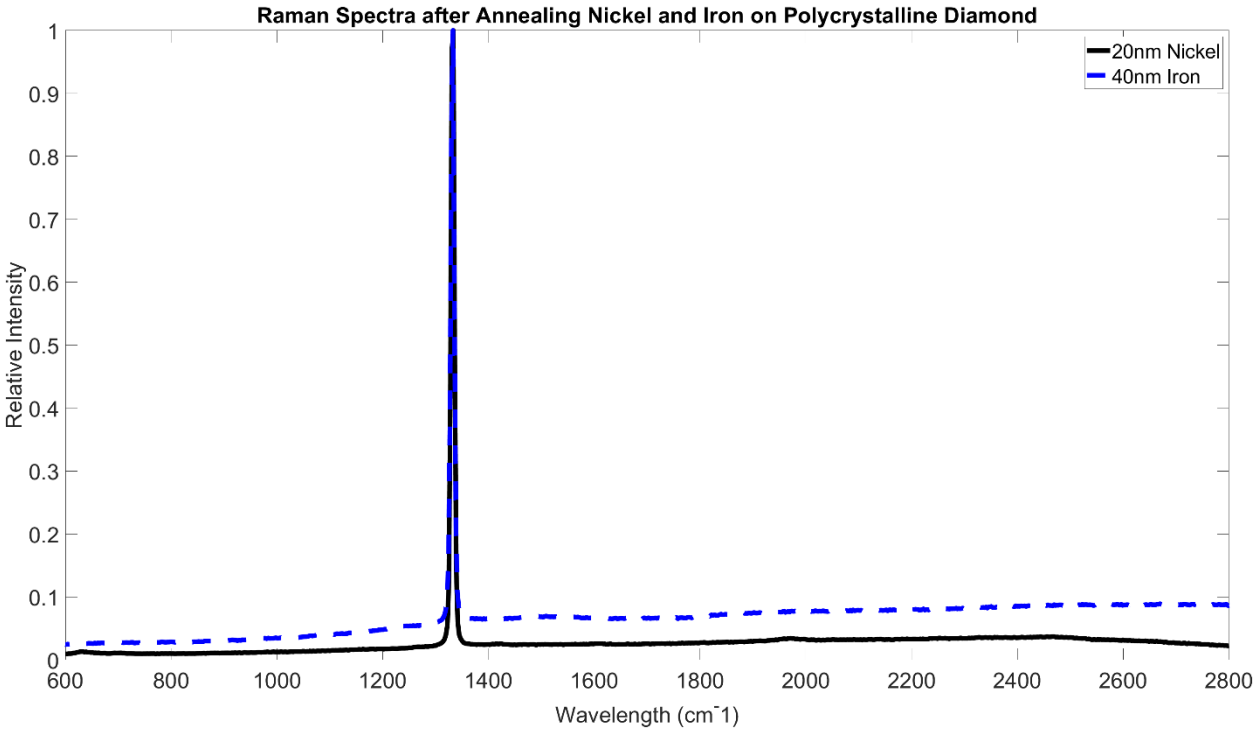

Figure 29: Raman spectra after heating nickel and iron on diamond to 800°C and 1050°C, respectively

3.5 Conclusion

Efforts to pyrolyze PNHC into diamond as well as graphitize ultrananocrystalline and polycrystalline diamond using metal catalysts are discussed in this study. Following the general synthesis procedure outlined in literature, a beige powder, assumed to be PNHC, was produced. This study outlines the synthesis procedure in detail. Attempts to pyrolyze the polymer into diamond, using the procedure widely used in relevant literature, failed because of poor environmental control. Attempts to graphitize ultrananocrystalline diamond also failed, most likely due to the incompatibility of the hot acid cleaning treatment as well as the burning of any diamond during the annealing process. The oxidizing or burning of diamond also prevented graphitization of polycrystalline diamond, with exception of the RTA of nickel on diamond. The

nickel on diamond annealing resulted in the growth of multilayer graphene with measure sheet carrier concentrations and hole mobilities of $1.0*10^{15}$ cm^{-2} and 629.1 cm^2 Vs^{-1}, which are higher than any reported values in literature.

3.6 Future Work

The poor environmental control during heating processes was identified as the most likely reason for the failure to synthesize diamond. The next steps proceeding this work begins with GPC analysis to determine the exact identity of the polymer and its molecular weight. NMR analysis will determine the purity of the polymer and presence of other elements and compounds in the powder. Next, a thin tube furnace and an adequate flow rates need to be employed for the pyrolysis and annealing procedures for the synthesis and graphitization efforts. Raman spectroscopy, profilometry, and AFM will give insights on resulting surface identification and physical characteristics. If both efforts are successful, testing metal catalysts to graphitize the diamond synthesized from PNHC pyrolysis will help determine the feasibility of manufacturing all-carbon electronics in an alternative method to CVD.

References

[1] Khanna, V. K. (2023). Extreme-temperature and harsh-environment electronics: physics, technology and applications. IOP Publishing.

[2] (2020) *Introduction to Wirewound Resistors*. Vishay Intertechnologies. https://static4.arrow.com/-/media/arrow/files/pdf/0320-wirewound-resistors-introduction.pdf?h=16&thn=1&w=16&hash=FA4F624DB8298D17A5B2660DDAF69EB9.

[3] Naefe, J. E., Johnson, R. W., & Grzybowski, R. R. (2002). High-temperature storage and thermal cycling studies of thick film and wirewound resistors. *IEEE Transactions on Components and Packaging Technologies*, 25(1), 45-52.

[4] Ebbert, P. (2014). The wirebound resistor:'the report of my death was an exaggeration Riedon White paper.

[5] Ho, J. S., & Greenbaum, S. G. (2018). Polymer capacitor dielectrics for high temperature applications. *ACS applied materials & interfaces*, *10*(35), 29189-29218.

[6] Barrow, D. A., Petroff, T. E., Tandon, R. P., & Sayer, M. (1997). Characterization of thick lead zirconate titanate films fabricated using a new sol gel based process. *Journal of Applied Physics*, *81*(2), 876-881.

[7] Dittmer, R., Anton, E. M., Jo, W., Simons, H., Daniels, J. E., Hoffman, M., ... & Rödel, J. (2012). A high-temperature-capacitor dielectric based on K 0.5 Na 0.5 NbO 3-modified Bi 1/2 Na 1/2 TiO 3–Bi 1/2 K 1/2 TiO 3. *Journal of the American Ceramic Society*, 95(11), 3519-3524.

[8] Lall, P., Yadav, V., Suhling, J., & Locker, D. (2019, May). Reliability of leadfree solders in high temperature vibration in automotive environments. *In 2019 18th IEEE Intersociety Conference on Thermal and Thermomechanical Phenomena in Electronic Systems* (ITherm) (pp. 566-585). IEEE.

[9] Jiang, N., Zhang, L., Liu, Z. Q., Sun, L., Long, W. M., He, P., ... & Zhao, M. (2019). Reliability issues of lead-free solder joints in electronic devices. *Science and technology of advanced materials*, *20*(1), 876-901.

[10] Zeng, G., McDonald, S., & Nogita, K. (2012). Development of high-temperature solders. *Microelectronics Reliability*, *52*(7), 1306-1322.

[11] Chidambaram, V., Hattel, J., & Hald, J. (2011). High-temperature lead-free solder alternatives. *Microelectronic Engineering*, *88*(6), 981-989.

[12] Suganuma, K., Kim, S. J., & Kim, K. S. (2009). High-temperature lead-free solders: Properties and possibilities. *JOM Journal of the Minerals, Metals and Materials Society*, *61*(1), 64.

[13] Soft Serve Die Attach. Indium Corporation. White paper.

[14] Chidambaram, V., Hald, J., & Hattel, J. (2010). Development of Au–Ge based candidate alloys as an alternative to high-lead content solders. *Journal of alloys and compounds*, *490*(1-2), 170-179.

[15] Liu, H., Xue, S., Tao, Y., Long, W., Zhong, S., & Wang, B. (2020). Study on the reliability of novel Au–30Ga solder for high-temperature packaging. *Journal of Materials Research and Technology*, *9*(6), 15908-15923.

[16] Yoon, J. W., Chun, H. S., Koo, J. M., Lee, H. J., & Jung, S. B. (2007). Microstructural evolution of Sn-rich Au–Sn/Ni flip-chip solder joints under high temperature storage testing conditions. *Scripta Materialia*, *56*(8), 661-664.

[17] Song, J. M., Chuang, H. Y., & Wu, Z. M. (2006). Interfacial reactions between Bi-Ag high-temperature solders and metallic substrates. *Journal of electronic materials*, *35*, 1041-1049.

[18] Shi, Y., Fang, W., Xia, Z., Lei, Y., Guo, F., & Li, X. (2010). Investigation of rare earth-doped BiAg high-temperature solders. *Journal of Materials Science: Materials in Electronics*, *21*, 875-881.

[19] Rettenmayr, M., Lambracht, P., Kempf, B., & Tschudin, C. (2002). Zn-Al based alloys as Pb-free solders for die attach. *Journal of electronic materials*, *31*, 278-285.

[20] Wang, C. H., Chen, H. H., & Li, P. Y. (2012). Interfacial reactions of high-temperature Zn–Sn solders with Ni substrate. Materials Chemistry and Physics, 136(2-3), 325-333.

[21] Yoon, S. W., Glover, M. D., & Shiozaki, K. (2012). Nickel–tin transient liquid phase bonding toward high-temperature operational power electronics in electrified vehicles. *IEEE Transactions on Power Electronics*, *28*(5), 2448-2456.

[22] Moeini, S. A., Greve, H., & McCluskey, F. P. (2014). Strength and reliability of high temperature transient liquid phase sintered joints. *Additional Papers and Presentations*, *2014*(HITEC), 000355-000363.

[23] Li, Z. L., Dong, H. J., Song, X. G., Zhao, H. Y., Feng, J. C., Liu, J. H., ... & Wang, S. J. (2017). Rapid formation of Ni3Sn4 joints for die attachment of SiC-based high temperature power devices using ultrasound-induced transient liquid phase bonding process. *Ultrasonics Sonochemistry*, *36*, 420-426.

[24] Shao, H., Wu, A., Bao, Y., Zhao, Y., Zou, G., & Liu, L. (2018). Thermal reliability investigation of Ag-Sn TLP bonds for high-temperature power electronics application. *Microelectronics Reliability, 91*, 38-45.

[25] Liu, J., Lv, W., Mou, Y., Peng, Y., Zhu, F., & Chen, M. (2023). Sn-enhanced high-temperature reliability of Cu/Nano-Ag/Cu joint via transient-liquid-phase bonding. *Journal of Materials Science*, 1-15.

[26] Greve, H., Chen, L. Y., Fox, I., & McCluskey, F. P. (2013, May). Transient liquid phase sintered attach for power electronics. In *2013 IEEE 63rd Electronic Components and Technology Conference* (pp. 435-440). IEEE.

[27] Greve, H., & McCluskey, F. P. (2014). LT-TLPS Die Attach for High Temperature Electronic Packaging. *Journal of Microelectronics and Electronic Packaging*, *11*(1), 7-15.

[28] Lee, J. B., Hwang, H. Y., & Rhee, M. W. (2015). Reliability investigation of Cu/In TLP bonding. *Journal of Electronic Materials*, *44*, 435-441.

[29] Mohan, K., Shahane, N., Raj, P. M., Antoniou, A., Smet, V., & Tummala, R. (2017, March). Low-temperature, organics-free sintering of nanoporous copper for reliable, high-temperature and high-power die-attach interconnections. In *2017 IEEE Applied Power Electronics Conference and Exposition (APEC)* (pp. 3083-3090). IEEE.

[30] Bhogaraju, S. K., Schmid, M., Hufnagel, E., Conti, F., Kotadia, H. R., & Elger, G. (2021, June). Low temperature and low pressure die-attach bonding of high power light emitting diodes with self reducing copper complex paste. In *2021 IEEE 71st Electronic Components and Technology Conference (ECTC)* (pp. 526-531). IEEE.

[31] Kraft, S., Schletz, A., & Maerz, M. (2012, March). Reliability of silver sintering on DBC and DBA substrates for power electronic applications. In *2012 7th International Conference on Integrated Power Electronics Systems (CIPS)* (pp. 1-6). IEEE.

[32] Tan, Y., Li, X., Chen, G., Gao, Q., Lu, G. Q., & Chen, X. (2020). Effects of thermal aging on long-term reliability and failure modes of nano-silver sintered lap-shear joint. *International Journal of Adhesion and Adhesives*, *97*, 102488.

[33] Nishimoto, S., Moeini, S. A., Ohashi, T., Nagatomo, Y., & McCluskey, P. (2018). Novel silver die-attach technology on silver pre-sintered DBA substrates for high temperature applications. *Microelectronics Reliability, 87*, 232-237.

[34] Bhogaraju, S. K., Mokhtari, O., Conti, F., & Elger, G. (2020). Die-attach bonding for high temperature applications using thermal decomposition of copper (II) formate with polyethylene glycol. *Scripta Materialia*, *182*, 74-80.

[35] Saccon, R., Bhogaraju, S. K., & Elger, G. (2022, November). Cu sintering for high power electronics packaging–challenges and solutions. In *Mikro-Nano-Integration; 9. GMM-Workshop* (pp. 1-6). VDE.

[36] Saccon, R., Benin, A., Bhogaraju, S. K., & Elger, G. (2022, May). Effect of binders on the performance of copper sintering pastes. In *2022 International Conference on Electronics Packaging (ICEP)* (pp. 71-72). IEEE.

[37] Zhang, B., Damian, A., Zijl, J., van Zeijl, H., Zhang, Y., Fan, J., & Zhang, G. (2021). In-air sintering of copper nanoparticle paste with pressure-assistance for die attachment in high power electronics. *Journal of Materials Science: Materials in Electronics*, *32*, 4544-4555.

[38] Yasui, K., Hayakawa, S., Nakamura, M., Kawase, D., Ishigaki, T., Sasaki, K., ... & Kobayashi, T. (2018, May). Improvement of power cycling reliability of 3.3 kV full-SiC power modules with sintered copper technology for T j, max= 175° C. In *2018 IEEE 30th International Symposium on Power Semiconductor Devices and ICs (ISPSD)* (pp. 455-458). IEEE.

[39] Suzuki, T., Yasuda, Y., Terasaki, T., Morita, T., Kawana, Y., Ishikawa, D., ... & Matsuda, T. (2019). Tensile-Fatigue Behavior of Sintered Copper Die-Attach Material. *IEEE Transactions on Device and Materials Reliability*, *19*(2), 461-467.

[40] Chen, T. F., & Siow, K. S. (2021). Comparing the mechanical and thermal-electrical properties of sintered copper (Cu) and sintered silver (Ag) joints. *Journal of alloys and Compounds*, *866*, 158783.

[41] Suzuki, T., Yasuda, Y., Terasaki, T., Morita, T., Kawana, Y., Ishikawa, D., ... & Kurafuchi, K. (2016, April). Thermal cycling lifetime estimation of sintered metal die attachment. In *2016 International Conference on Electronics Packaging (ICEP)* (pp. 400-404). IEEE.

[42] Schnabl, K., Wentlent, L., Mootoo, K., Khasawneh, S., Zinn, A. A., Beddow, J., ... & Borgesen, P. (2014). Nanocopper based solder-free electronic assembly. *Journal of Electronic Materials*, *43*, 4515-4521.

[43] Suzuki, T., Yasuda, Y., Terasaki, T., Morita, T., Kawana, Y., Ishikawa, D., ... & Matsuda, T. (2018, December). Evaluation of Microscopic Strain Distribution of Low-Temperature Sintering Die Attach in Thermal Cycling Test. In *2018 20th International Conference on Electronic Materials and Packaging (EMAP)* (pp. 1-4). IEEE.

[44] Furukawa, T., Shiraishi, M., Yasuda, Y., Konno, A., Mori, M., Morita, T., ... & Kawase, D. (2017, May). High power density side-gate HiGT modules with sintered Cu having superior high-temperature reliability to sintered Ag. In *2017 29th International Symposium on Power Semiconductor Devices and IC's (ISPSD)* (pp. 263-266). IEEE.

[45] Sakamoto, S., Sugahara, T., & Suganuma, K. (2013). Microstructural stability of Ag sinter joining in thermal cycling. *Journal of Materials Science: Materials in Electronics*, *24*, 1332-1340.

[46] Gao, Y., Takata, S., Chen, C., Nagao, S., Suganuma, K., Bahman, A. S., & Iannuzzo, F. (2019). Reliability analysis of sintered Cu joints for SiC power devices under thermal shock condition. *Microelectronics Reliability*, *100*, 113456.

[47] Ishikawa, D., Nakako, H., Kawana, Y., Sugama, C., Negishi, M., Ejiri, Y., ... & Weber, M. (2018, September). Copper die-bonding sinter paste: Sintering and bonding properties. In *2018 7th Electronic System-Integration Technology Conference (ESTC)* (pp. 01-10). IEEE.

[48] Wang, Y., Watanabe, A. O., Ogura, N., Raj, P. M., & Tummala, R. (2020). Sintered nanocopper paste for high-performance 3D heterogeneous package integration. *Journal of Electronic Materials*, *49*, 6737-6745.

[49] Chasserio, N., Guillemet, S., Lebey, T., & Dagdag, S. (2009). Ceramic substrates for high-temperature electronic integration. *Journal of Electronic Materials*, *38*(1), 164-174.

[50] Khazaka, R., Mendizabal, L., Henry, D., & Hanna, R. (2014). Survey of high-temperature reliability of power electronics packaging components. *IEEE Transactions on power Electronics*, *30*(5), 2456-2464.

[51] Hamilton, D. P., Riches, S., Meisser, M., Mills, L., & Mawby, P. (2016, March). High temperature thermal cycling performance of DBA, AMB and thick film power module substrates. In *CIPS 2016; 9th International Conference on Integrated Power Electronics Systems* (pp. 1-5). VDE.

[52] Ning, P., Lai, R., Huff, D., Wang, F., Ngo, K. D., Immanuel, V. D., & Karimi, K. J. (2009). SiC wirebond multichip phase-leg module packaging design and testing for harsh environment. *IEEE Transactions on Power Electronics*, *25*(1), 16-23.

[53] Katsis, D. C., & Zheng, Y. (2008, June). Development of an extreme temperature range silicon carbide power module for aerospace applications. In *2008 IEEE Power Electronics Specialists Conference* (pp. 290-294). IEEE.

[54] Fukumoto, A., Berry, D., Ngo, K. D., & Lu, G. Q. (2014). Effects of Extreme Temperature Swings (-40 to 250 C) on Silicon Nitride Active Metal Brazing Substrates. IEEE transactions on device and materials reliability, 14(2), 751-756.

[55] Miyazaki, H., Iwakiri, S., Hirao, K., Fukuda, S., Izu, N., Yoshizawa, Y. I., & Hyuga, H. (2017). Effect of high temperature cycling on both crack formation in ceramics and delamination of copper layers in silicon nitride active metal brazing substrates. *Ceramics International*, *43*(6), 5080-5088.

[56] Miyazaki, H., Zhou, Y., Iwakiri, S., Hirotsuru, H., Hirao, K., Fukuda, S., ... & Hyuga, H. (2018). Improved resistance to thermal fatigue of active metal brazing substrates for silicon carbide power modules using tough silicon nitrides with high thermal conductivity. *Ceramics International*, *44*(8), 8870-8876.

[57] Lei, T. G., Calata, J. N., Ngo, K. D., & Lu, G. Q. (2009). Effects of large-temperature cycling range on direct bond aluminum substrate. *IEEE Transactions on Device and Materials Reliability*, *9*(4), 563-568.

[58] Tang, J., Mak, C. H. H., Tam, S. K., & Ng, K. M. (2021). Formulation of a paste for copper thick film. *Journal of Nanoparticle Research*, *23*(8), 166.

[59] Gundel, P., Nowak, T., Bawohl, M., Challingsworth, M., Czwickla, C., Garcia, V., ... & Shahbazi, C. (2016, March). Thermal Performance and Reliability of Copper Thick Film Substrates. In *CIPS 2016; 9th International Conference on Integrated Power Electronics Systems* (pp. 1-6). VDE.

[60] Hopkins, D. C. (2019). Trends in Power Electronics Packaging.

[61] Mehrotra, U., Cheng, T. H., Kanale, A., Agarwal, A., Han, K., Baliga, B. J., ... & Hopkins, D. C. (2020, September). Packaging development for a 1200V SiC BiDFET switch using highly thermally conductive organic epoxy laminate. In *2020 32nd International Symposium on Power Semiconductor Devices and ICs (ISPSD)* (pp. 396-399). IEEE.

[62] Kanale, A., Cheng, T. H., Narwal, R., Agarwal, A., Baliga, B. J., Bhattacharya, S., & Hopkins, D. C. (2022, October). Design Considerations for Developing 1.2 kV 4H-SiC BiDFET-enabled Power Conversion Systems. In *2022 IEEE Energy Conversion Congress and Exposition (ECCE)* (pp. 1-7). IEEE.

[63] Cheng, T. H., Nishiguchi, K., Fukawa, Y., Baliga, B. J., Bhattacharya, S., & Hopkins, D. C.

[64] Kim, I., Cho, S., Jung, D., Lee, C. R., Kim, D., & Baek, B. J. (2013). Thermal analysis of high power LEDs on the MCPCB. *Journal of Mechanical Science and Technology*, *27*, 1493-1499.

[65] Pounds, D., & Bonner, R. W. (2014, May). High heat flux heat pipes embedded in metal core printed circuit boards for LED thermal management. In *Fourteenth Intersociety Conference on Thermal and Thermomechanical Phenomena in Electronic Systems (ITherm)* (pp. 267-271). IEEE.

[66] Horng, R. H., Hong, J. S., Tsai, Y. L., Wuu, D. S., Chen, C. M., & Chen, C. J. (2010). Optimized thermal management from a chip to a heat sink for high-power GaN-based light-emitting diodes. *IEEE transactions on electron devices*, *57*(9), 2203-2207.

[67] Kyatam, S., Rodrigues, L., Maslovski, S., Alves, L. N., & Mendes, J. C. (2022). Improving the reliability of power LEDs with diamond boards. *Diamond and Related Materials*, *127*, 109144.

[68] Hantos, G., Juhász, L., & Rencz, M. (2014, September). In situ thermal reliability testing methodology for novel thermal interface materials. In *20th International Workshop on Thermal Investigations of ICs and Systems* (pp. 1-5). IEEE.

[69] Gurpinar, E., Ozpineci, B., & Chowdhury, S. (2020). Design, analysis, comparison, and experimental validation of insulated metal substrates for high-power wide-bandgap power modules. *Journal of Electronic Packaging*, *142*(4).

[70] Gurpinar, E., Chowdhury, S., Ozpineci, B., & Fan, W. (2020). Graphite-embedded high-performance insulated metal substrate for wide-bandgap power modules. *IEEE Transactions on Power Electronics*, *36*(1), 114-128.

[71] Lu, J. L., Chen, D., & Yushyna, L. (2017, October). A high power-density and high efficiency insulated metal substrate based GaN HEMT power module. In *2017 IEEE Energy Conversion Congress and Exposition (ECCE)* (pp. 3654-3658). IEEE.

[72] Mohan, S. (2019). Thermal Comparison of FR-4 and Insulated Metal Substrate PCB for GaN Inverter. *Texas Instruments: Dallas, TX, USA*.

[73] Lee, C. C., Kao, K. S., Wang, C. W., Yu, T. J., Lee, T. K., & Chiu, P. K. (2022). Assembly Reliability and Molding Material Comparison of Miniature Integrated High Power Module With Insulated Metal Substrate. *Journal of Electronic Packaging*, *144*(2).

[74] (2023). Integrated circuits for temperatures up to 300 °C. *Fraunhofer Institute for Microelectronic Circuits and Systems*. Website. https://www.ims.fraunhofer.de/en/Core-Competence/Technology/Special-Technology/High-Temperature-Technology.html#:~:text=The%20high%2Dtemperature%20technology%20of,300%20%C2%B0C%20operating%20temperature.

[75] Koizumi, S., Umezawa, H., Pernot, J., & Suzuki, M. (Eds.). (2018). *Power electronics device applications of diamond semiconductors*. Woodhead publishing.

[76] Paramanik, B., & Das, D. (2022). Synthesis of nanocrystalline diamond embedded diamond-like carbon films on untreated glass substrates at low temperature using (C2H2+ H2) gas composition in microwave plasma CVD. *Applied Surface Science*, *579*, 152132.

[77] Kumar, R. "Enhancing Performance and Reliability if High Temperature Electronics through Thermally-Stable Parylene HT," Proceedings of the International Conference on High Temperature Electronics, May 13-15, 2014, Albuquerque, NM, pp. 256-262.

[78] Sezer Hicyilmaz, A., & Celik Bedeloglu, A. (2021). Applications of polyimide coatings: A review. *SN Applied Sciences*, *3*, 1-22.

[79] Khmelnitsky, R. A., & Gippius, A. A. (2014). Transformation of diamond to graphite under heat treatment at low pressure. *Phase Transitions, 87*(2), 175-192.

[80] Neudeck, P. G., Okojie, R. S., & Chen, L. Y. (2002). High-temperature electronics-a role for wide bandgap semiconductors?. *Proceedings of the IEEE, 90*(6), 1065-1076.

[81] *Diamond, Natural*. MatWeb. (n.d.).

[82] Kasu, M. (2016). Diamond epitaxy: Basics and applications. *Progress in Crystal Growth and Characterization of Materials, 62*(2), 317-328.

[83] Bovenkerk, H. P., Bundy, F. P., Hall, H. T., Strong, H. M., & Wentorf, R. H. (1959). Preparation of diamond. *Nature, 184*(4693), 1094-1098.

[84] Sumiya, H., & Satoh, S. (1996). High-pressure synthesis of high-purity diamond crystal. *Diamond and Related Materials, 5*(11), 1359-1365.

[85] Li, Y., Wang, C., Chen, L., Guo, L., Zhang, Z., Fang, C., & Ma, H. (2019). An effective method to improve the growth rate of large single crystal diamonds under HPHT processes: optimized design of the catalyst geometric construction. *RSC advances, 9*(55), 32205-32209.

[86] Sumiya, H., Harano, K., & Tamasaku, K. (2015). HPHT synthesis and crystalline quality of large high-quality (001) and (111) diamond crystals. *Diamond and related materials, 58*, 221-225.

[87] Guignard, J., Prakasam, M., & Largeteau, A. (2022). A review of binderless polycrystalline diamonds: Focus on the high-pressure–high-temperature sintering process. *Materials, 15*(6), 2198.

[88] Li, Q., Zhan, G., Li, D., He, D., Moellendick, T. E., Gooneratne, C. P., & Alalsayednassir, A. G. (2020). Ultrastrong catalyst-free polycrystalline diamond. *Scientific Reports, 10*(1), 22020.

[89] Osipov, V. Y., Shakhov, F. M., Bogdanov, K. V., Takai, K., Hayashi, T., Treussart, F., ... & Jentgens, C. (2020). High-quality green-emitting nanodiamonds fabricated by HPHT sintering of polycrystalline shockwave diamonds. *Nanoscale Research Letters, 15*, 1-13.

[90] Chen, C., & Chen, Q. (2008). Recent development in diamond synthesis. *International Journal of Modern Physics B, 22*(04), 309-326.

[91] Sawaoka, A. B., Takamatsu, M., & Akashi, T. (1994). Shock compression synthesis of diamond. *Advanced Materials, 6*(5), 346-354.

[92] Schwander, M., & Partes, K. (2011). A review of diamond synthesis by CVD processes. *Diamond and related materials, 20*(9), 1287-1301.

[93] Din, S. H., Shah, M. A., Sheikh, N. A., & Butt, M. M. (2019). CVD diamond. *transactions of the Indian Institute of Metals*, *72*, 1-9.

[94] Wang, X., Zhao, T., Sun, F., & Shen, B. (2015). Comparisons of HFCVD diamond nucleation and growth using different carbon sources. *Diamond and Related Materials*, *54*, 26-33.

[95] Yu, Z., & Flodström, A. (1997). Pressure dependence of growth mode of HFCVD diamond. *Diamond and related materials*, *6*(1), 81-84.

[96] Barbosa, D. C., Almeida, F. A., Silva, R. F., Ferreira, N. G., Trava-Airoldi, V. J., & Corat, E. J. (2009). Influence of substrate temperature on formation of ultrananocrystalline diamond films deposited by HFCVD argon-rich gas mixture. *Diamond and Related Materials*, *18*(10), 1283-1288.

[97] Tzeng, Y., Phillips, R., Cutshaw, C., Srivinyunon, T., Loo, B. H., & Wang, P. (1991). Multiple flame deposition of diamond films. *Applied physics letters*, *58*(23), 2645-2647.

[98] Baek, S. H., Mihec, D. F., & Metson, J. B. (2002). The Deposition of Diamond Films by Combustion Assisted CVD on Ti and Ti-6Al-4V. *Chemical Vapor Deposition*, *8*(1), 29-34.

[99] Butler, J. E., Mankelevich, Y. A., Cheesman, A., Ma, J., & Ashfold, M. N. R. (2009). Understanding the chemical vapor deposition of diamond: recent progress. *Journal of Physics: Condensed Matter*, *21*(36), 364201.

[100] Rosenkranz, B., & Bettmer, J. (2000). Microwave-induced plasma–optical emission spectrometry–fundamental aspects and applications in metal speciation analysis. *TrAC Trends in Analytical Chemistry*, *19*(2-3), 138-156.

[101] Morgan, C. G. (1975). Laser-induced breakdown of gases. *Reports on Progress in Physics*, *38*(5), 621.

[102] Jonkers, J., De Regt, J. M., Van der Mullen, J. A. M., Vos, H. P. C., De Groote, F. P. J., & Timmermans, E. A. H. (1996). On the electron temperatures and densities in plasmas produced by the "torche à injection axiale". *Spectrochimica Acta Part B: Atomic Spectroscopy*, *51*(11), 1385-1392.

[103] Berghaus, J. O., Meunier, J. L., & Gitzhofer, F. (1998). Diamond coatings for tool shafts by induction plasma deposition. *International Journal of Refractory Metals and Hard Materials*, *16*(3), 201-205.

[104] Metev, S., Stephen, A., Schwarz, J., & Wochnowski, C. (2003). Laser-induced chemical micro-treatment and synthesis of materials. *Riken Review*, 47-52.

[105] Kamo, M., Sato, Y., Matsumoto, S., & Setaka, N. (1983). Diamond synthesis from gas phase in microwave plasma. *Journal of crystal growth*, *62*(3), 642-644.

[106] Pleuler, E., Wild, C., Füner, M., & Koidl, P. (2002). The CAP-reactor, a novel microwave CVD system for diamond deposition. *Diamond and related materials*, *11*(3-6), 467-471.

[107] Ohtake, N., & Yoshikawa, M. (1990). Diamond film preparation by arc discharge plasma jet chemical vapor deposition in the methane atmosphere. *Journal of the Electrochemical Society*, *137*(2), 717.

[108] Lu, F. X., Zhong, G. F., Sun, J. G., Fu, Y. L., Tang, W. Z., Wang, J. J., ... & Zhang, Y. G. (1998). A new type of DC arc plasma torch for low cost large area diamond deposition. *Diamond and related Materials*, *7*(6), 737-741.

[109] Hirata, A., & Yoshikawa, M. (1995). Effects of electrode arrangement and pressure on synthesis of diamond films by arc discharge plasma jet chemical vapor deposition. *Diamond and related materials*, *4*(12), 1363-1370.

[110] Arnault, J. C., Saada, S., & Ralchenko, V. (2022). Chemical vapor deposition single-crystal diamond: a review. *physica status solidi (RRL)–Rapid Research Letters*, *16*(1), 2100354.

[111] Thomas, E. L., Mandal, S., Brousseau, E. B., & Williams, O. A. (2014). Silica based polishing of {100} and {111} single crystal diamond. *Science and technology of advanced materials*

[112] Achard, J., Tallaire, A., Mille, V., Naamoun, M., Brinza, O., Boussadi, A., ... & Gicquel, A. (2014). Improvement of dislocation density in thick CVD single crystal diamond films by coupling H2/O2 plasma etching and chemo-mechanical or ICP treatment of HPHT substrates. *physica status solidi (a)*, *211*(10), 2264-2267.

[113] Tavares, C., Koizumi, S., & Kanda, H. (2005). Effects of RIE treatments for {111} diamond substrates on the growth of P-doped diamond thin films. *physica status solidi (a)*, *202*(11), 2129-2133.

[114] Schuelke, T., & Grotjohn, T. A. (2013). Diamond polishing. *Diamond and Related Materials*, *32*, 17-26.

[115] Grillo, S. E., & Field, J. E. (1997). The polishing of diamond. *Journal of Physics D: Applied Physics*, *30*(2), 202.

[116] Tallaire, A., Barjon, J., Brinza, O., Achard, J., Silva, F., Mille, V., ... & Gicquel, A. (2011). Dislocations and impurities introduced from etch-pits at the epitaxial growth resumption of diamond. *Diamond and Related Materials*, *20*(7), 875-881.

[117] Watanabe, J., Touge, M., & Sakamoto, T. (2013). Ultraviolet-irradiated precision polishing of diamond and its related materials. *Diamond and related materials*, *39*, 14-19.

[118] De Sio, A., Di Fraia, M. I. C. H. E. L. E., Antonelli, M., Menk, R. H., Cautero, G. I. U. S. E. P. P. E., Carrato, S. E. R. G. I. O., ... & Pace, E. (2013). X-ray micro beam analysis of the photoresponse of an enlarged CVD diamond single crystal. *Diamond and related materials*, *34*, 36-40.

[119] Widmann, C. J., Müller-Sebert, W., Lang, N., & Nebel, C. E. (2016). Homoepitaxial growth of single crystalline CVD-diamond. *Diamond and Related Materials*, *64*, 1-7.

[120] Zhang, L., Wei, Q., An, J., Ma, L., Zhou, K., Ye, W., ... & Luo, J. (2020). Construction of 3D interconnected diamond networks in Al-matrix composite for high-efficiency thermal management. *Chemical Engineering Journal*, *380*, 122551.

[121] Mehmel, L., Issaoui, R., Brinza, O., Tallaire, A., Mille, V., Delchevalrie, J., ... & Achard, J. (2021). Dislocation density reduction using overgrowth on hole arrays made in heteroepitaxial diamond substrates. *Applied Physics Letters*, *118*(6).

[122] Mandal, S. (2021). Nucleation of diamond films on heterogeneous substrates: a review. *RSC advances*, *11*(17), 10159-10182.

[123] Arblaster, J. W. (2010). Crystallographic properties of iridium. *Platinum Metals Review*, *54*(2), 93-102.

[124] Robertson, J. J. S. M. K. H., Gerber, J., Sattel, S., Weiler, M., Jung, K., & Ehrhardt, H. (1995). Mechanism of bias-enhanced nucleation of diamond on Si. *Applied physics letters*, *66*(24), 3287-3289.

[125] Arnault, J. C., Saada, S., Michaelson, S., Hangaly, N. K., Akhvlediani, R., & Hoffman, A. (2008). Bias enhanced diamond nucleation onto 3C–SiC (100) surfaces studied by high resolution X-ray photoelectron and high resolution electron energy loss spectroscopies. *Diamond and related materials*, *17*(3), 377-382.

[126] Kono, S., Goto, T., Abukawa, T., Wild, C., Koidl, P., & Kawarada, H. (2000). Surface order evaluation of the heteroepitaxial diamond film grown on an inclined β-SiC (001). *Japanese Journal of Applied Physics*, *39*(7S), 4372.

[127] Fei, W., Wei, K., Morishita, A., Wang, H., & Kawarada, H. (2020). Local initial heteroepitaxial growth of diamond (111) on Ru (0001)/c-sapphire by antenna-edge-type microwave plasma chemical vapor deposition. *Applied Physics Letters*, *117*(11).

[128] Sumiya, H., & Tamasaku, K. (2012). Large defect-free synthetic type IIa diamond crystals synthesized via high pressure and high temperature. *Japanese journal of applied physics*, *51*(9R), 090102.

[129] Lebedev, V., Engels, J., Kustermann, J., Weippert, J., Cimalla, V., Kirste, L., ... & Sittinger, V. (2021). Growth defects in heteroepitaxial diamond. *Journal of Applied Physics*, *129*(16).

[130] Stehl, C., Fischer, M., Gsell, S., Berdermann, E., Rahman, M. S., Traeger, M., ... & Schreck, M. (2013). Efficiency of dislocation density reduction during heteroepitaxial growth of diamond for detector applications. *Applied Physics Letters*, *103*(15).

[131] Schreck, M., Mayr, M., Klein, O., Fischer, M., Gsell, S., Sartori, A. F., & Gallheber, B. C. (2016). Multiple role of dislocations in the heteroepitaxial growth of diamond: A brief review. *physica status solidi (a)*, *213*(8), 2028-2035.

[132] Stoner, 1., Ma, G. H., Wolter, S. D., & Glass, J. T. (1992). Characterization of bias-enhanced nucleation of diamond on silicon by invacuo surface analysis and transmission electron microscopy. *Physical Review B*, *45*(19), 11067.

[133] Arnault, J. C., Saada, S., Delclos, S., Rocha, L., Intiso, L., Polini, R., ... & Bergonzo, P. (2008). Surface Science Contribution to the BEN Control on Si (100) and 3C-SiC (100): Towards Ultrathin Nanocrystalline Diamond Films. *Chemical vapor deposition*, *14*(7-8), 187-195.

[134] Ichikawa, K., Kurone, K., Kodama, H., Suzuki, K., & Sawabe, A. (2019). High crystalline quality heteroepitaxial diamond using grid-patterned nucleation and growth on Ir. *Diamond and Related Materials*, *94*, 92-100.

[135] Yamasaki, S., Gheeraert, E., & Koide, Y. (2014). Doping and interface of homoepitaxial diamond for electronic applications. *Mrs Bulletin*, *39*(6), 499-503.

[136] Ohmagari, S., Ogura, M., Umezawa, H., & Mokuno, Y. (2017). Lifetime and migration length of B-related admolecules on diamond {1 0 0}-surface: comparative study of hot-filament and microwave plasma-enhanced chemical vapor deposition. *Journal of Crystal Growth*, *479*, 52-58.

[137] Takano, Y., Nagao, M., Takenouchi, T., Umezawa, H., Sakaguchi, I., Tachiki, M., & Kawarada, H. (2005). Superconductivity in polycrystalline diamond thin films. *Diamond and related materials*, *14*(11-12), 1936-1938.

[138] Kubovic, M., & Kasu, M. (2010). Enhancement and stabilization of hole concentration of hydrogen-terminated diamond surface using ozone adsorbates. *Japanese Journal of Applied Physics*, *49*(11R), 110208.

[139] Nesladek, M. (2005). Conventional n-type doping in diamond: state of the art and recent progress. *Semiconductor Science and Technology*, *20*(2), R19.

[140] Kalish, R., Reznik, A., Prawer, S., Saada, D., & Adler, J. (1999). Ion-implantation-induced defects in diamond and their annealing: experiment and simulation. *physica status solidi (a), 174*(1), 83-99.

[141] Prins, J. F. (1991). Annealing effects when activating dopant atoms in ion-implanted diamond layers. *Nuclear Instruments and Methods in Physics Research Section B: Beam Interactions with Materials and Atoms*, *59*, 1387-1390.

[142] J.F. Ziegler, J.P. Biersack, U. Littmark (1985), The Stopping and Range of Ions in Solids, Pergamon, New York, NY.

[143] Prins, J. F. (1989). Preparation of ohmic contacts to semiconducting diamond. *Journal of Physics D: Applied Physics*, *22*(10), 1562.

[144] Abubakr, E., Ohmagari, S., Zkria, A., Ikenoue, H., & Yoshitake, T. (2022). Laser-induced novel ohmic contact formation for effective charge collection in diamond detectors. *Materials Science in Semiconductor Processing*, *139*, 106370.

[145] Schreck, M., Gsell, S., Brescia, R., & Fischer, M. (2017). Ion bombardment induced buried lateral growth: the key mechanism for the synthesis of single crystal diamond wafers. *Scientific reports*, *7*(1), 44462.

[146] Mokuno, Y., Chayahara, A., Soda, Y., Yamada, H., Horino, Y., & Fujimori, N. (2006). High rate homoepitaxial growth of diamond by microwave plasma CVD with nitrogen addition. *Diamond and related materials*, *15*(4-8), 455-459.

[147] Vescan, A., Daumiller, I., Gluche, P., Ebert, W., & Kohn, E. (1997). Very high temperature operation of diamond Schottky diode. *IEEE Electron Device Letters*, *18*(11), 556-558.

[148] Koné, S., Schneider, H., Isoird, K., Thion, F., Achard, J., Issaoui, R., ... & Alexis, J. (2012). An assessment of contact metallization for high power and high temperature diamond Schottky devices. *Diamond and related materials*, *27*, 23-28.

[149] Eon, D., Traoré, A., Pernot, J., & Gheeraert, E. E. (2016, June). Recent progress on diamond Schottky diode. In *2016 28th International Symposium on Power Semiconductor Devices and ICs (ISPSD)* (pp. 55-58). IEEE.

[150] Tatsumi, N., Ikeda, K., Umezawa, H., & Shikata, S. (2009). Development of diamond Schottky barrier diode. *SEI Technical review*, *68*, 54.

[151] Sasama, Y., Kageura, T., Imura, M., Watanabe, K., Taniguchi, T., Uchihashi, T., & Takahide, Y. (2022). High-mobility p-channel wide-bandgap transistors based on hydrogen-terminated diamond/hexagonal boron nitride heterostructures. *Nature Electronics*, *5*(1), 37-44.

[152] Kawarada, H., Tsuboi, H., Naruo, T., Yamada, T., Xu, D., Daicho, A., ... & Hiraiwa, A. (2014). CH surface diamond field effect transistors for high temperature (400 C) and high voltage (500 V) operation. *Applied physics letters*, *105*(1).

[153] Vescan, A., Gluche, P., Ebert, W., & Kohn, E. (1997). High-temperature, high-voltage operation of pulse-doped diamond MESFET. *IEEE Electron Device Letters*, *18*(5), 222-224.

[154] Iwasaki, T., Hoshino, Y., Tsuzuki, K., Kato, H., Makino, T., Ogura, M., ... & Hatano, M. (2013). High-temperature operation of diamond junction field-effect transistors with lateral pn junctions. *IEEE Electron Device Letters*, *34*(9), 1175-1177.

[155] Bianconi, P. A., Joray, S. J., Aldrich, B. L., Sumranjit, J., Duffy, D. J., Long, D. P., ... & Babyak, J. M. (2004). Diamond and diamond-like carbon from a preceramic polymer. *Journal of the American Chemical Society*, *126*(10), 3191-3202.

[156] Bulychev, B. M., Zvukova, T. M., Sizov, A. I., Aleksandrov, A. F., Korobov, Y. A., Kanzyuba, M. V., & Khomich, A. V. (2010). Poly (naphthalenehydrocarbyne): synthesis, characterization, and application to preparation of thin diamond films. *Russian Chemical Bulletin*, *59*, 1724-1728.

[157] Nur, Y., Cengiz, H. M., Pitcher, M. W., & Toppare, L. K. (2009). Electrochemical polymerizatıon of hexachloroethane to form poly (hydridocarbyne): a pre-ceramic polymer for diamond production. *Journal of materials science*, *44*, 2774-2779.

[158] BAŞMAN, N., ERGEN, S., ALKAN, C., & Orhan, U. Z. U. N. (2019). Characterization of a diamond-like carbon film produced from an electrosynthesized pre-ceramic polymer. *Journal of New Results in Science*, *8*(2), 74-81.

[159] Katzenmeyer, A. M., Bayam, Y., VJ, L., Pitcher, M. W., Nur, Y., Seyyidoğlu, S., ... & Islam, M. S. (2009). Poly (hydridocarbyne) as Highly Processable Insulating Polymer Precursor to Micro/Nanostructures and Graphite Conductors. *Journal of Nanomaterials*, *2009*.

[160] Sedov, V. S., Ralchenko, V. G., Zvukova, T. M., & Sizov, A. I. (2017). Polycarbynes: A new synthetic approach and application to the nucleation of CVD diamond. *Diamond and Related Materials*, *74*, 65-69.

[161] Nam, H. (2019). Electrochemical polymerization of various halogenated hydrocarbons.

[162] Ichibha, T., Hongo, K., Motochi, I., Makau, N. W., Amolo, G. O., & Maezono, R. (2018). Adhesion of electrodes on diamond (111) surface: A DFT study. *Diamond and Related Materials*, *81*, 168-175.

[163] Drozdov, M. N., Demidov, E. V., Drozdov, Y. N., Kraev, S. A., Shashkin, V. I., Arkhipova, E. A., ... & Bogdanov, S. A. (2019). Formation of low-resistivity Au/Mo/Ti ohmic contacts to p-diamond epitaxial layers. *Technical Physics*, *64*, 1827-1836.

[164] Moazed, K. L., Nguyen, R., & Zeidler, J. R. (1988). Ohmic contacts to semiconducting diamond. *IEEE electron device letters*, *9*(7), 350-351.

[165] Nakanishi, J., Otsuki, A., Oku, T., Ishiwata, O., & Murakami, M. (1994). Formation of ohmic contacts to p-type diamond using carbide forming metals. *Journal of Applied Physics*, *76*(4), 2293-2298.

[166] Chen, Y., Ogura, M., Yamasaki, S., & Okushi, H. (2005). Ohmic contacts on p-type homoepitaxial diamond and their thermal stability. *Semiconductor science and technology*, *20*(8), 860.

[167] Drozdov, M. N., Arkhipova, E. A., Drozdov, Y. N., Kraev, S. A., Shashkin, V. I., Parafin, A. E. E., ... & Bogdanov, S. A. (2020). The use of pulsed laser annealing to form ohmic Mo/Ti contacts to diamond. *Technical Physics Letters*, *46*, 551-555.

[168] Lei, L., Su, Y., Bolzoni, L., & Yang, F. (2020). Evaluation on the interface characteristics, thermal conductivity, and annealing effect of a hot-forged Cu-Ti/diamond composite. *Journal of Materials Science & Technology*, *49*, 7-14.

[169] Matsumoto, T., Kato, H., Tokuda, N., Makino, T., Ogura, M., Takeuchi, D., ... & Yamasaki, S. (2014). Reduction of n-type diamond contact resistance by graphite electrode. *physica status solidi (RRL)–Rapid Research Letters*, *8*(2), 137-140.

[170] Evans, T., & James, P. F. (1964). A study of the transformation of diamond to graphite. *Proceedings of the Royal Society of London. Series A. Mathematical and Physical Sciences*, *277*(1369), 260-269.

[171] Fedoseev, D. V., Vnukov, S. P., Bukhovets, V. L., & Anikin, B. A. (1986). Surface graphitization of diamond at high temperatures. *Surface and Coatings Technology*, *28*(2), 207-214.

[172] Cooil, S. P., Song, F., Williams, G. T., Roberts, O. R., Langstaff, D. P., Jørgensen, B., … Wells, J. W. (2012). *Iron-mediated growth of epitaxial graphene on SiC and diamond. Carbon, 50(14), 5099–5105.* doi:10.1016/j.carbon.2012.06.050.

[173] Okotrub, A. V., Gorodetskiy, D. V., Palyanov, Y. N., Smirnov, D. A., & Bulusheva, L. G. (2023). Iron-catalyzed growth of vertical graphitic layers on the (100) face of single-crystal diamond. *The Journal of Physical Chemistry C*, *127*(7), 3563-3569.

[174] Romanyuk, O., Varga, M., Tulic, S., Izak, T., Jiricek, P., Kromka, A., ... & Rezek, B. (2018). Study of Ni-catalyzed graphitization process of diamond by in situ X-ray photoelectron spectroscopy. *The Journal of Physical Chemistry C*, *122*(12), 6629-6636.

[175] Suntornwipat, N., Aitkulova, A., Djurberg, V., & Majdi, S. (2023). Rapid direct growth of graphene on single-crystalline diamond using nickel as catalyst. *Thin Solid Films*, *770*, 139766.

[176] Kanada, S., Nagai, M., Ito, S., Matsumoto, T., Ogura, M., Takeuchi, D., ... & Tokuda, N. (2017). Fabrication of graphene on atomically flat diamond (111) surfaces using nickel as a catalyst. *Diamond and Related Materials*, *75*, 105-109.

[177] Berman, D., Deshmukh, S. A., Narayanan, B., Sankaranarayanan, S. K., Yan, Z., Balandin, A. A., ... & Sumant, A. V. (2016). Metal-induced rapid transformation of diamond into single and multilayer graphene on wafer scale. *Nature communications*, *7*(1), 1-8.

[178] Ueda, K., Aichi, S., & Asano, H. (2016). Direct formation of graphene layers on diamond by high-temperature annealing with a Cu catalyst. *Diamond and Related Materials*, *63*, 148-152.

[179] Tulić, S., Waitz, T., Čaplovičová, M., Habler, G., Vretenár, V., Susi, T., & Skákalová, V. (2021). Catalytic graphitization of single-crystal diamond. *Carbon*, *185*, 300-313.

[180] Zvukova, T. M., Sizov, A. I., & Bulychev, B. M. (2016). Improved synthesis of polycarbynes. *Mendeleev Communications*, *2*(26), 127-128.

[181] Nur, Y., Pitcher, M. W., Seyyidoğlu, S., & Toppare, L. (2008). Facile synthesis of poly (hydridocarbyne): a precursor to diamond and diamond-like ceramics. *Journal of Macromolecular Science, Part A*, *45*(5), 358-363.

[182] Prawer, S., Nugent, K. W., Jamieson, D. N., Orwa, J. O., Bursill, L. A., & Peng, J. L. (2000). The Raman spectrum of nanocrystalline diamond. *Chemical Physics Letters*, *332*(1-2), 93-97.

[183] Birrell, J., Gerbi, J. E., Auciello, O., Gibson, J. M., Johnson, J., & Carlisle, J. A. (2005). Interpretation of the Raman spectra of ultrananocrystalline diamond. *Diamond and Related Materials*, *14*(1), 86-92.

[184] Brown, K. J., Chartier, E., Sweet, E. M., Hopper, D. A., & Bassett, L. C. (2019). Cleaning diamond surfaces using boiling acid treatment in a standard laboratory chemical hood. *Journal of Chemical Health & Safety*, *26*(6), 40-44.

[185] Sartori, A. F., Overes, B. H., Fanzio, P., Tsigkourakos, M., Sasso, L., & Buijnsters, J. G. (2019). Template-assisted bottom-up growth of nanocrystalline diamond micropillar arrays. *Diamond and Related Materials*, *95*, 20-27.